Durham Research Online

Additional information:

Crossing the Eddington Limit: Examining Disk Spectra at High Accretion Rates

Andrew D. Sutton[1], Douglas A. Swartz[1], Timothy P. Roberts[2], Matthew J. Middleton[3],
Roberto Soria[4,5], and Chris Done[2]

[1] Astrophysics Office, NASA Marshall Space Flight Center, ZP12, Huntsville, AL 35812, USA; andrew.d.sutton@nasa.gov
[2] Centre for Extragalactic Astronomy, Department of Physics, Durham University, South Road, Durham, DH1 3LE, UK
[3] Institute of Astronomy, University of Cambridge, Madingley Road, Cambridge, CB3 0HA, UK
[4] International Centre for Radio Astronomy Research, Curtin University, GPO Box U1987, Perth, WA 6845, Australia
[5] Sydney Institute for Astronomy, School of Physics A28, The University of Sydney, Sydney, NSW 2006, Australia

Abstract

The faintest ultraluminous X-ray sources (ULXs), those with 0.3–10 keV luminosities $1 < L_X/10^{39} < 3$ erg s^{-1}, tend to have X-ray spectra that are disk-like but broader than expected for thin accretion disks. These "broadened disk (BD)" spectra are thought to indicate near- or mildly super-Eddington accretion onto stellar remnant black holes. Here we report that a sample of bright thermal-dominant black hole binaries, which have Eddington ratios constrained to moderate values, also show BD spectra in the 0.3–10 keV band at an order of magnitude lower luminosities. This broadening would be missed in studies that only look above ~2 keV. While this may suggest that BD ULXs could be powered by accretion onto massive stellar remnant black holes with close to maximal spin, we argue in favor of a scenario where they are at close to the Eddington luminosity, such that radiation pressure would be expected to result in geometrically slim, advective accretion disks. However, this implies that an additional physical mechanism is required to produce the observed broad spectra at low Eddington ratios.

Key words: accretion, accretion disks – black hole physics – X-rays: binaries

1. Introduction

Ultraluminous X-ray sources (ULXs) are non-nuclear point sources in external galaxies that are primarily defined by their extraordinarily high X-ray luminosities of $L_X \geqslant 10^{39}$ erg s^{-1}. To produce such extreme luminosities, most ULXs are presumably powered by accretion onto black holes (although as of writing three have been reported to contain neutron stars; Bachetti et al. 2014; Fuerst et al. 2016; Israel et al. 2016a, 2016b). This lower limit in luminosity is close to the Eddington luminosity, $L_{Edd} \sim 1.3 \times 10^{39}$ erg s^{-1}, of a typical ~10 $M_\odot$ stellar-mass black hole. Thus, ULXs must contain larger black holes and/or have higher Eddington ratios, $l \equiv L/L_{Edd}$, than we commonly see in Galactic black hole binaries (BHBs).

There are several well-defined accretion states of Galactic BHBs that tend to occur within certain ranges of (sub-) Eddington ratios. For instance, quiescence and the hard state have similar properties (a hard power-law spectrum with a cutoff at a few tens of keV) and occur at $l \ll 1$ (although the hard state has been reported to peak at high fractions of the Eddington luminosity, $l \lesssim 0.7$, during a few outbursts; Dunn et al. 2010). On the other hand, the thermal-dominant (TD) state typically occurs at higher Eddington ratios, $0.1 \lesssim l \lesssim 0.3$. BHBs are also observed in a less well understood steep power law state, which is characterized by a power-law spectrum with $\Gamma > 2.4$ and occurs at both higher and lower luminosity than the TD state (for more in-depth reviews of sub-Eddington accretion states see, e.g., McClintock & Remillard 2006; Remillard & McClintock 2006; Done et al. 2007). Thus, it was initially hoped that rudimentary constraints could be placed on Eddington ratios, and hence black hole masses, in ULXs based on their energy spectra alone, if they were in standard sub-Eddington states.

However, most of the highest-quality ULX spectra show near-ubiquitous high-energy curvature at around 5 keV, which

is often coupled to a soft excess (Stobbart et al. 2006; Gladstone et al. 2009; Bachetti et al. 2013; Walton et al. 2014). We note that a TD spectrum could appear as an absorbed cutoff power law, without a soft excess, in the ~0.3–10 keV band. However, TD-like spectra can be rejected for many ULXs, and the high black hole masses implied by sub-Eddington states are often inconsistent with the $\geqslant 1$ keV disk temperatures obtained when ULX spectra are fitted with disk models (e.g., Gladstone et al. 2009). Exceptions to this may include the least luminous ULXs (e.g., a 30 $M_\odot$ black hole in the TD state at $0.3L_{Edd}$ would have a bolometric luminosity of ~1.2×10^{39} erg s^{-1} and a disk spectrum peaking at ~1 keV; Shakura & Sunyaev 1973).

This combination of a soft excess and high-energy curvature, along with the high luminosities, is unlike any known sub-Eddington state, leading to the suggestion of a new accretion state, which is generally termed the "ultraluminous state" (Gladstone et al. 2009). The ultraluminous state has been further subdivided into three distinctive spectral types, which we now refer to as the broadened disk (BD), hard ultra-luminous, and soft ultraluminous regimes (Sutton et al. 2013). The luminosity of the majority of BD ULXs ($\lesssim 3 \times 10^{39}$ erg s^{-1}) is such that they bridge the gap between the sub-Eddington BHBs and the hard and soft ultraluminous sources, which has led to the suggestion that they may represent accretion at $l \sim 1$, while ULXs in the hard and soft ultraluminous regimes, seen almost exclusively at luminosities above ~3×10^{39} erg s^{-1}, likely represent super-Eddington mass accretion rates (Sutton et al. 2013). Hard and soft ultraluminous sources have two distinct spectral components that may indicate the presence of radiatively driven outflows in the supercritical accretion regime; the disk-like spectra in BD sources could perhaps be intermediate in shape between these two-component spectra and a disk-only spectrum (Middleton et al. 2011, 2012).

Sub-Eddington TD spectra are dominated by emission from a geometrically thin accretion disk, which can be approximated by a multicolor disk (MCD) model (plus a faint high-energy power-law tail; e.g., McClintock & Remillard 2006). As $l \rightarrow 1$, radiation pressure would be expected to cause the disk scale height to increase; thus, advection should start to become important (e.g., Abramowicz et al. 1988; Watarai et al. 2001; Sądowski 2009), giving rise to the so-called slim disks with spectra that are subtly broader than the TD state, perhaps consistent with the BD ULX state (a steep power-law state has been reported between the thin- and slim-disk regimes in XTE 1550−564, but this is short-lived; Kubota & Makishima 2004). Recently it has been noted that some $l < 1$ TD BHBs have spectra that are subtly broader than even the best current thin-disk models. For example, BHSPEC (Davis et al. 2005) includes both the changing color temperature correction due to atomic features and relativistic effects, and it is intrinsically broader than KERRBB (relativistic effects, but constant color temperature correction) or an MCD (no relativistic effects and a constant color temperature correction; see Done & Davis 2008). Nonetheless, *Suzaku* spectra of LMC X-3 (Kubota et al. 2010) and *XMM-Newton* spectra of GX 339−4 (Kolehmainen et al. 2011) are broader than can be reproduced by the BHSPEC disk model. Kolehmainen et al. (2011) show that the spectra of GX 339−4 are best fitted by two-component phenomenological models that are strikingly similar to those used to argue in favor of two-component spectra in many ULXs, namely, a low-temperature MCD plus cool, optically thick Comptonization (e.g., Gladstone et al. 2009). Similarly, unusual broadening is seen in a transient ULX in M31 (Straub et al. 2013; M31 ULX1 in this study). This source has a spectrum that is well fitted by slim-disk models when it is at ULX luminosities and in the BD regime. Interestingly, as this source faded to lower luminosities, its spectrum remained unusually broad, such that standard thin-disk models were unable to provide a good fit to the data.

Further similarities between the TD BHBs and BD ULXs are evident from fitting irradiated disk models to X-ray and optical data. In BHBs, X-rays from the inner regions of the accretion disk irradiate the outer disk, where they are reprocessed and re-emitted as optical/UV emission at the local blackbody temperature (Gierliński et al. 2008, 2009). As thin disks transit to slim disks with increasing Eddington ratio, the fraction of emission that is reprocessed would be expected to decrease, due to self-shielding in the accretion disk (Kaaret & Corbel 2009). However, it has been reported that BD ULXs have similar reprocessing fractions to the TD BHBs, suggesting that their geometries may not be vastly different (Sutton et al. 2014).

Clearly something is missing from our understanding of accretion disks. Motivated by the possible similarities between sub-Eddington TD BHBs and potentially approximately Eddington BD ULXs, we here present a comparison of TD and BD sources. Historically, Galactic BHBs and ULXs have mainly been studied with different instruments (e.g., *Rossi X-ray Timing Explorer* [*RXTE*] and *XMM-Newton*/*Chandra*, respectively), which crucially have different bandpasses. Although external galaxies have been observed in the ∼0.3–10 keV range (e.g., Vulic et al. 2016), the net counts obtained from binaries are generally not sufficient to allow spectral studies comparable to those that are possible in Galactic BHBs, or even nearby ULXs. There are also additional complications coming from the difficulties in distinguishing

BHBs from neutron star binaries. This bandpass mismatch presents serious, but often overlooked, limitations in comparisons between the two source classes, as subtle broadening may not be evident if disk spectra are only observed above 2 keV. As such, we here assess high count rate ∼0.3–10 keV CCD spectra of nearby BHBs (of known black hole mass) to establish whether they can truly be described by TD models while at substantially sub-Eddington luminosities or if an additional component, especially broadening, is required. Comparison is also made to more luminous (but poorer spectral quality) ULXs in nearby galaxies to better understand the accretion physics and Eddington ratio giving rise to the BD ULX state. We describe the selection of our TD and BD samples in Section 2, outline the tests we carry out in Section 3, present our findings in Section 4, and discuss the implications of these in the context of the broader literature in Section 5.

2. Sample Selection

The intention of this work was to compare BD ULXs with high mass accretion rate BHBs. As such, we considered CCD observations in the ∼0.3–10 keV energy range of BHBs with $l \gtrsim 0.1$. Although BHBs are occasionally detected in a bright "steep power-law" state (e.g., Remillard & McClintock 2006), this state is characterized by a power-law-like spectrum, while the TD state appears most comparable to the BD ULXs. We therefore concentrated on the TD BHBs in this work.

We defined a sample of BHB observations taken from the 21 BHBs with known masses out to the distance of the LMC from Zhang (2013). This contains the same 20 confirmed BHBs as Remillard & McClintock (2006), with the addition of H1743 −322. We obtained mission-long 1-day-average *RXTE* All-Sky Monitor (ASM) light curves from the ASM Web page[6] for all of the sources. The maximum *RXTE* ASM count rate for each source was used to extrapolate an estimate of the peak Eddington ratio ($l_{0.3-10\,keV} \approx L_{0.3-10\,keV}/(M_{BH} \times 1.3 \times 10^{38}\,erg\,s^{-1}\,M_{\odot}^{-1})$) using PIMMS,[7] assuming a 1 keV blackbody-shaped spectrum. We emphasize that this model is just a rough approximation of a thermal spectrum that we used to define our sample, and we would not expect it to be appropriate for accurately extrapolating *RXTE* fluxes to the 0.3–10 keV band, especially in spectra with strong power-law components. We also note that we here define the Eddington ratio in terms of the 0.3–10 keV luminosity. While the bolometric correction for an absorbed 1 keV blackbody observed in the 0.3–10 keV range is only ∼1%, larger corrections would be expected for more realistic spectra (e.g., Migliari & Fender 2006 reported $L_{2-10\,keV}/L_{Bol} \sim 0.8$ for outbursting BHBs, albeit in a narrower energy band). We did not correct luminosities for inclination in an accretion disk. This is motivated by the lack of good inclination estimates in many sources, especially the ULXs. However, we do note the approximate correction factors for the BHBs in the final sample (Table 1), and for most estimates of their inclinations this is only a factor of 0.5–1.5.

For BHBs that exceeded $l \approx 0.1$ in the ASM light curves, we searched the High Energy Astrophysics Science Archive Research Center (HEASARC) archive[8] for *Swift* and *XMM-Newton* detections. Five sources had *XMM-Newton* and/or *Swift* detections during time periods where the ASM light

---

Table 1
The BHB Sample

Source ID[a]	M_{BH}[b] ($M_\odot$)	Reference	Distance[c] (kpc)	Reference	N_H[d] (10^{20} cm^{-2})	l[e]	i[f] (deg)	Reference	$1/(2\cos i)$[g]
GX 339−4	7.5 ± 0.8	1	∼8	4	…	0.2	20–30, >45	5, 6	0.5–0.6, >0.7
LMC X-3	6.98 ± 0.56	2	48 ± 2	3	4.68	0.9	∼70	7	∼1.5
LMC X-1	10.91 ± 1.41	3	48 ± 2	3	6.73	0.7	∼36	3	∼0.6

Notes.
[a] Common source name.
[b] Black hole mass.
[c] Distance to the BHB.
[d] Galactic neutral hydrogen column density in the direction of the LMC sources from Dickey & Lockman (1990); no value is given for GX 339−4 as it is within our Galaxy.
[e] Approximate Eddington ratio ($L_{0.3-10\,keV}/(M_{BH} \times 1.3 \times 10^{38}$ erg s^{-1} $M_\odot^{-1}$)) at the peak *RXTE* ASM count rate for an assumed absorbed 1 keV blackbody shaped spectrum.
[f] Inclination of the binary system.
[g] Approximate correction factor between apparent luminosity and the luminosity of an accretion disk.
References. (1) Chen 2011 (note that this mass estimate is based on a scaling of the spectral and timing properties, but it is in agreement with the mass function derived from the radial velocity curve, $f(M_{BH}) = 5.8 \pm 0.5$ $M_\odot$; Hynes et al. 2003); (2) Orosz et al. 2014; (3) Orosz et al. 2009; (4) Zdziarski et al. 2004; (5) Miller et al. 2004; (6) Kolehmainen & Done 2010; (7) Orosz et al. 2014.

Table 2
BHB Observation Log

Instrument/Mode[a]	ObsID[b]	Date[c]	t_{exp}[d] (ks)	Count Rate[e] (s^{-1})	$\log_{10}(f_X)$[f] ($\log_{10}$(erg cm^{-2} s^{-1}))	l[g]
			GX 339−4			
XMM-B	0093562701 (*XMM*-1)	2002 Aug 24	1.3	5.2×10^3	−7.548 ± 0.002	0.22
XMM-B	0410581201 (*XMM*-2)	2007 Feb 19	0.4	5.2×10^3	−7.554 ± 0.003	0.22
			LMC X-3			
XMM-T	0109090101 (*XMM*-1)	2000 Nov 24	9.2	420	−8.784 ± 0.002	0.46
Swift-WT	00037080006 (*Swift*-1)	2007 Dec 02	9.2	25	−9.037 ± 0.001	0.25
XMM-T	0671420301 (*XMM*-2)	2011 May 27	8.0	250	−9.028 ± 0.004	0.26
			LMC X-1			
XMM-T	0112900101 (*XMM*-1)	2000 Oct 21	4.9	120	−9.07 ± 0.01	0.16
Swift-WT	00037079002 (*Swift*-1)	2007 Dec 06	9.8	14	−9.05 ± 0.03	0.17
Swift-WT	00037079003 (*Swift*-2)	2007 Dec 10	4.4	15	−9.09 ± 0.03	0.16

Notes.
[a] Instrument with which the observations were taken—*XMM-Newton* EPIC in timing (*XMM*-T) or burst (*XMM*-B) mode, or *Swift* XRT in window timing mode (*Swift*-WT).
[b] *XMM-Newton* or *Swift* observation identification number.
[c] Observation start date.
[d] Effective good exposure time.
[e] Net source count rate (to two significant figures).
[f] Logarithm of the unabsorbed 0.3–10 keV flux averaged over the observation calculated from the XSPEC model TBABS × (DISKBB + COMPTT) using the CFLUX convolution model.
[g] Approximate Eddington ratio ($l_{0.3-10\,keV}$).

curves indicated that they met our Eddington ratio selection criteria. These were GRO 1655−40, GX 339−4, GRS 1915+104, LMC X-3, and LMC X-1.

We excluded GRS 1915+104 from our sample, as its strong absorption column ($N_H \sim 4 \times 10^{22}$ cm^{-2}; Ebisawa 1998) makes detailed study of this source difficult below 2 keV. Additionally, GRO 1655−40 had a single *Swift* XRT observation in low rate photodiode mode that met our Eddington ratio criteria, but it also had a strong power-law component in its spectrum, even below 10 keV. This was also the case in *XMM-Newton* observations 0410581301 and

0023940401 of GX 339−4 and LMC X-1, respectively. As these three observations deviated from disk-dominated spectra, we do not consider them further. Details of the remaining BHB sample are given in Table 1,[9] and an observation log is given in Table 2. Although they were not initially flagged as such, it later became apparent that LMC X-1 *Swift*-1 and *Swift*-2 may also have deviated from a strictly TD state, so caution must be

---

[9] A distance of ∼50 kpc to the LMC is currently preferred (Pietrzyński et al. 2013; de Grijs et al. 2014; Crandall & Ratra 2015), but we use 48 kpc here for consistency with the Orosz et al. (2009) mass estimate of LMC X-1.

Table 3
The ULX Sample

Source ID[a]	XMM/CXO ID[b]	Distance[c] (Mpc)	N_H[d] (10^{20} cm^{-2})	ObsID[e]	t_{exp}[f] (ks)	Count rate[g] (s^{-1})
M31 ULX2	XMMU J004243.6+412519	0.79	6.85	0674210601	15.1/18.6/18.8	0.65/0.59/0.54
M31 ULX1	CXOM31 J004253.1+411422	0.79	6.68	0600660201	14.5/⋯/⋯	6.2/⋯/⋯
NGC 253 XMM2	2XMM J004722.6−252050	3.68	1.38	0152020101	55.9/76.1/76.8	0.25/0.083/0.084
NGC 253 ULX2	2XMM J004732.9−251749	3.68	1.38	0152020101	56.0/76.1/76.8	0.22/0.075/0.074
M33 X-8	2XMM J013350.8+303937	0.92	5.69	0650510201	61.1/⋯/⋯	4.5/⋯/⋯
NGC 2403 X-1	2XMM J073625.5+653540	3.50	4.17	0164560901	50.8/69.3/72.4	0.29/0.099/0.10
NGC 4736 ULX1	2XMM J125048.6+410743	4.66	1.44	0404980101	32.7/42.9/43.3	0.26/0.076/0.078

Notes.
[a] Common source name, which in the case of M31 ULX2 has not been used previously, but it is defined here for convenience.
[b] Catalog identifier of the source.
[c] Distance to the source.
[d] Galactic neutral hydrogen column density in the direction of the ULX from Dickey & Lockman ([1990]).
[e] *XMM-Newton* observation identifier of the data sets used in this work, all of which were taken in full frame imaging mode.
[f] Good exposure time in ks for the EPIC pn/MOS1/MOS2 detectors; ellipsis points indicate that data from the corresponding detector were not used in this study.
[g] Count rate for the EPIC pn/MOS1/MOS2 detector.

used when interpreting these (see Section [4.5.1]). Of the remaining sources, GX 339−4 is a variable Galactic low-mass X-ray binary (LMXB) and LMC X-3 and X-1 are high-mass X-ray binaries (HMXBs) in the Large Magellanic Cloud. Despite LMC X-3 being an HMXB, it likely accretes via Roche lobe overflow (Soria et al. [2001]). On the other hand, LMC X-1 is thought to accrete via a stellar wind (Orosz et al. [2009]), but it is unusual as it has a stable accretion disk. We note that Ruhlen & Smith ([2010]) have suggested that it may be a hybrid Roche lobe overflow/wind accretion system.

The main purpose of this work was to compare the most luminous TD sub-Eddington BHBs with a sample of BD ULXs. As such, we defined a ULX sample as those sources identified as having BD spectra and 0.3–10 keV X-ray luminosities $<3 \times 10^{39}$ erg s^{-1} by Sutton et al. ([2013]). To these we add another ULX in M31 (M31 ULX2), which is a transient that at its peak had an unabsorbed X-ray luminosity of $\sim 1.3 \times 10^{39}$ erg s^{-1} (Middleton et al. [2013]). For each source we consider only the observation with the highest-quality data in either Sutton et al. ([2013]) or Middleton et al. ([2013]), details of which are given in Table [3]. The observations chosen for M31 ULX1 and ULX2 were the most luminous reported by these authors, and that chosen for NGC 253 XMM2 was close to the peak luminosity. The NGC 253 ULX2 and M33 X-8 observations were below peak luminosity, and only single observations of both NGC 2403 X-1 and NGC 4736 ULX1 were reported in Sutton et al. ([2013]). Out of the ULX sample, three sources have been reported to be transients: M31 ULX2 (Barnard et al. [2013]; Middleton et al. [2013]), M31 ULX1 (Kaur et al. [2012]; Middleton et al. [2012]), and NGC 4736 ULX1 (Akyuz et al. [2013]). The other four ULXs are consistently detected in previous observations, so they are potentially persistent or long-period transient sources (e.g., Schlegel & Pannuti [2003]; Sutton et al. [2013], [2014]; La Parola et al. [2015]). Given their X-ray luminosities, the ULXs are most likely powered by Roche lobe overflow. Faint ULXs may be either HMXBs or LMXBs (Swartz et al. [2004]), although it has been argued that ULXs are predominantly HMXBs (e.g., King et al. [2001]).

3. Analysis

We extracted X-ray spectra for all of the *XMM-Newton* and *Swift* observations in Tables [2] and [3]. *XMM-Newton* spectra were extracted using Science Analysis Software (SAS) version 14.0.0.[10] We considered only the EPIC pn data for the high-flux TD BHBs, although EPIC pn, MOS1, and MOS2 data were all used for the lower-flux ULXs. The pn and MOS observation data files were processed using EPPROC and EMPROC, respectively. Full-field high-energy (>10 keV) light curves were extracted and used to define good time intervals (GTIs), using TABGTIGEN, to filter out periods of high background flaring.

The definition of source and background regions differed between the ULXs and BHBs. For the BHB observations, which were in timing and burst mode, rectangular source regions were defined in raw CCD coordinates. These spanned 18 pixels in RAW-X centered on the source "streak" in the raw coordinate image. For observations in timing mode the full range of RAW-Y was used. For the burst mode observations pixels with RAW-Y greater than 140 were excluded (Kirsch et al. [2006]). Sources with count rates $\gtrsim 200$ s^{-1} dominate the events over the entire *XMM-Newton* EPIC pn CCD in some bands, even in timing modes.[11] As a result of this, there is no uncontaminated region from which to extract a background spectrum. Simply approximating a background spectrum defined at the edge of the CCD would modify the source spectrum in at least some bands as the point-spread function is energy dependent (Done & Diaz Trigo [2010]). Therefore, it is recommended not to subtract any background at all (Ng et al. [2010]). As such, the only *XMM-Newton* BHB observation for which we extracted a background spectrum is *XMM*-1 of LMC X-1, where the count rate is lower than 200 s^{-1}. In this case, the background was defined in a region spanning RAW-X = 3–5. The TD BHB source and background spectra were extracted using EVSELECT with standard pattern and flag selections (PATTERN $\leqslant 4$ and FLAG = 0). The task BACKSCALE was used to add the BACKSCAL keyword to the

---
[10] http://xmm.esac.esa.int/sas/
[11] http://xmm2.esac.esa.int/docs/documents/CAL-TN-0083.pdf

headers of the source and background spectra from LMC X-1 to account for different source and background region sizes.

For the ULX observations, which are in imaging mode, source spectra were extracted from circular regions centered on the sources, with typical radii of $\sim 30''$, although smaller regions were used for NGC 253 ULX2 ($10''$), NGC 4736 ULX1 ($20''$), and the pn detection of NGC 253 XMM2 ($25''$) due to neighboring sources or proximity to chip gaps. Background spectra were extracted from larger circular regions (typically $\gtrsim 30''$ for pn and $\gtrsim 50''$ for MOS1/2). For the MOS exposures, these were defined in source-free regions on the same chip as the source. In ideal cases, pn background spectra were extracted from source-free regions on the same chip as the source at similar distances from the readout node. Where this was not possible, backgrounds were extracted from neighboring CCDs in the same quadrant as the source and at a similar distance from the readout node. In the pn detection of M33 X-8, following the above prescription and defining a background region in a source-free area of a neighboring CCD in the same quadrant resulted in undersubtraction of the Cu/Ni detector line complex at ~ 8 keV. As such, for this source we compromised by extracting the background spectrum from the same CCD as the source, but at a slightly larger distance from the readout node. A comparison of this and a standard background defined on the neighboring chip demonstrated that the final spectra did not differ significantly outside of the energy range of the Cu/Ni detector lines. Spectra were extracted using EVSELECT with the recommended FLAG and PATTERN options (PATTERN $\leqslant 4$ and FLAG $= 0$ for pn, and PATTERN $\leqslant 12$ and the #XMMEA_EM flag selection for MOS), and BACKSCALE was used to add the BACKSCAL keyword to the headers of the source and background spectra.

Redistribution matrix files (RMFs) and ancillary response files (ARFs) were generated using RMFGEN and ARFGEN for all of the BHB and ULX *XMM-Newton* observations. Source and, in cases where they could be extracted, background spectra were associated with the appropriate RMFs and ARFs and then binned to a minimum of 20 counts using SPECGROUP. For the BHB observations we also set the oversample parameter to 3 to avoid oversampling the energy resolution of EPIC pn due to the high fluxes. During the processing of the ULX observations, a check of the event pattern distributions indicated that M31 ULX1 and M33 X-8 were slightly piled up. As such, we generated RMFs with pileup corrections[12] for the pn data from these sources and excluded the MOS exposures for which such corrections are not yet available in SAS.

Swift XRT spectra were extracted using XSELECT from events files with default selection criteria (i.e., grade 0–2 events for windowed timing mode). Source and background spectra were extracted from circular regions, and the values of the BACKSCAL keyword were manually changed such that they reflected the one-dimensional size of the regions. The appropriate RMF for windowed timing mode and grade 0–2 events was used from the calibration database, and ARFs were created for each observation using XRTMKARF with exposure maps from the pipeline data reduction. Finally, spectra and response files were grouped and binned to a minimum of 20 counts per bin using GRPPHA. We do not include an additional 3% fractional error, as is recommended to account for systematic uncertainties in *Swift* XRT spectra, since these are

not random errors and are likely correlated. As such, the systematic uncertainties in the instrument response were reflected in the value of χ^2 when fitting these spectra.

To minimize the effects of very different signal-to-noise ratios in the nearby BHBs and relatively distant ULXs, we undersampled each of the real BHB spectra to obtain realizations with $\sim 2.5 \times 10^4$ counts. We did this using a PYTHON script, which first normalized each of the unbinned source spectra such that they contained a total of 2.5×10^4 counts (and, where appropriate, applied the same normalization factor to the corresponding background spectrum), and then used the number of counts in each energy channel of the normalized spectra as expectation values to generate random numbers of counts from Poisson distributions. The random numbers of counts were used to construct the resampled spectra. These were then binned to a minimum of 20 counts and grouped with the corresponding resampled background spectra (where appropriate), RMFs, and ARFs using GRPPHA. As the exposure times were not altered in the header files, an additional multiplicative constant was included in the subsequent spectral fitting to account for the renormalization in flux. This was set equal to the ratio of the number of source counts in the simulated and real data.

Once extracted, the BHB (both real and resampled) and ULX spectra were read in to XSPEC v12.8.2 (Arnaud 1996) and fitted with various models in the 0.3–10 keV (*XMM-Newton* imaging mode and *Swift* observations) or 0.7–10 keV (*XMM-Newton* timing and burst mode observations) energy ranges, using abundances from Wilms et al. (2000) and photoionization absorption cross sections from Balucinska-Church & McCammon (1992), with a new He cross section based on Yan et al. (1998). Five spectral models were used, which we discuss in detail in the following section. For the extragalactic sources (i.e., all sources except for GX 339−4) an additional TBABS absorption component was included, which was fixed to the Galactic column density in the direction of the source (Tables 1 and 3). For fits to NGC 253 ULX2 an additional 0.67 keV MEKAL component was included, which was subject to Galactic absorption only, to account for diffuse emission around the source (see Sutton et al. 2013). Further details of the specific models and results from the spectral fitting are given in Section 4.

In addition to the spectral analysis, we also carried out a timing analysis. We extracted covariance spectra to test whether they were consistent with being constant and thus could originate from single-component energy spectra. Covariance is advantageous here over the raw rms variability, as by design the uncorrelated white noise cancels out, which reduces the statistical error. We calculated covariances in the time domain (Wilkinson & Uttley 2009) over timescales of 200 s to 7 ks. This choice of timescale was driven by the typical ULX count rates and observation lengths. It was not possible to study variability on these timescales in the *Swift* observations of LMC X-3 and LMC X-1 due to the orbit of the observatory, so these were excluded from this analysis. We note that the method of extracting covariance in the time domain (instead of frequency) could be affected by time lags. However, the timescales that we probed were much greater than lags expected in BHBs and reported in NGC 5408 X-1 (Heil & Vaughan 2010; De Marco et al. 2013, albeit in a more luminous ULX with a distinct two-component X-ray spectrum), although we caution that Hernández-García et al. (2015)

---

[12] http://xmm.esac.esa.int/sas/current/documentation/threads/epatplot.shtml

tentatively identified $\sim$1 ks lags below frequencies of 1 mHz at low significance in the same source.

Before covariances could be calculated, we needed to extract suitable light curves from each of the observations. For several of the ULXs the GTIs that we used for the spectral extraction contained many short periods of isolated good time, so we created new GTIs for these with binning and time limits chosen such that they were suitable for extracting simultaneous light curves in all of the EPIC detectors with multiple segments of 7 ks length. Source and, for the ULXs and LMC X-1, background light curves were extracted using EVSELECT. As we would be combining light curves from multiple detectors for the ULXs, fixed start and stop times were explicitly set for each observation. The light curves were corrected for, e.g., background, dead time, and quantum efficiency using EPICLC-CORR. Short gaps that occurred in the corrected light curves, due to zero good exposure time within a temporal bin, were filled by averaging over neighboring bins. For the ULXs the light curves from each detector in a given observation were summed to produce combined EPIC light curves. Finally, the light curves were rebinned to 200 s. Initially, we produced light curves in five energy bins equally sized in log space between 0.3 and 10 keV for each observation. If any of the light curves for a given observation contained fewer than $\sim$20 counts per 200 s bin on average, then the number of energy bins was reduced by one and the process repeated.

For each of the combined EPIC light curves, fractional rms variability was calculated in the time domain in 7 ks continuous segments, following Vaughan et al. (2003), and then averaged over the multiple segments. Where variability was detected at $\geqslant 3\sigma$ significance in at least one energy band, we went on to calculate covariance. The energy band with the most significant detection of fractional rms was used as the reference band. Covariances were normalized by $1/\sqrt{\sigma_{\mathrm{xs,y}}^2}$ (Wilkinson & Uttley 2009), where $\sigma_{\mathrm{xs,y}}^2$ is the excess variance in the reference band, and then divided by the mean count rate in the band of interest to obtain fractional covariances. These were again averaged over the multiple 7 ks segments. Where there were fewer than four light-curve segments we calculated the error on the covariance following Wilkinson & Uttley (2009); otherwise, we used standard errors. Once extracted, the fractional covariance spectra were fitted with constants.

4. Results

Various spectral models were fitted to the TD BHB and BD ULX data. These included models of pure thin accretion disks as well as physically motivated and phenomenological models of BDs. Examples of these are shown in Figure 1, and details follow. Uncertainties are quoted at the equivalent of 1σ significance throughout, and we reject models where the null hypothesis probability is greater than 0.997 (equivalent to 3σ significance).

4.1. MCD

The first model used to fit the TD BHB and BD ULX X-ray spectra was of an absorbed MCD, which is an approximation of a thin accretion disk with only two free parameters: disk temperature and normalization. Fit statistics and model parameters are reported in Table 4. A thin disk alone was rejected in the majority of BHB and ULX observations, with the exceptions of subsampled XMM-1 and XMM-2 of GX 339

−4, NGC 253 ULX2, and NGC 2403 X-1. Although the MCD model could not be statistically rejected for the subsampled GX 339−4 observations, alternative two-component models and a broad-disk model (DISKPBB in XSPEC) resulted in improved fit statistics (see below).

4.2. MCD Plus Power Law

The second model was of an absorbed MCD plus a power law. This model has two additional parameters compared to the MCD alone: the power-law spectral index and its normalization. Sutton et al. (2013) used this model to classify ULXs into the three spectral types. They defined BD ULXs as having inner-disk temperatures of greater than 0.5 keV and a 0.3–1 keV power law—MCD flux ratios of less than 5. We emphasize that this model is intended to be phenomenological in the BD ULXs, with the power law broadening the disk spectrum rather than fitting to a physically distinct component. The model parameters, fit statistics, and 0.3–1 keV component flux ratios for the observed BHB, resampled BHB, and ULX spectra are given in Table 5. The fit statistics indicate that the model was insufficient to reproduce the complex spectra from the complete BHB data, except in LMC X-1 Swift-2, which had some of the lowest-quality data among the complete BHB observations. The model could not be rejected for 6/8 of the resampled BHBs and 5/7 ULXs. Notably, the model was rejected for the resampled LMC X-1 Swift-2 spectrum, but it was marginally acceptable for the real data from this source. This is likely due to statistical effects when resampling the data.

All of the sources had best-fitting inner-disk temperatures greater than 0.5 keV. Also, in all sources where errors were estimated cooler accretion disks were rejected at $>3\sigma$ significance. All of the spectra also had 0.3–1 keV observed power-law–MCD flux ratios that were at least consistent with being less than or equal to 5, with greater values being strongly rejected ($>3\sigma$ significance) for four of the resampled BHB spectra and all of the ULXs. As such, we were rather predictably able to confirm that all of the ULXs selected for having BD spectra indeed have spectra that are broader than an MCD. But, crucially, this spectral model also indicated that some of the brightest TD BHBs had BD-shaped spectra at X-ray luminosities an order of magnitude lower than the ULXs.

Interestingly, although they are only approximate, the inner-disk radii calculated from the model normalizations appear to be a factor of $\sim$2 greater in the ULXs than the BHBs. If this corresponds to the innermost stable circular orbit, then it would indicate that the black holes in the BD ULXs were larger than in these TD BHBs.

4.3. MCD Plus Comptonization

The next model fitted to the TD and BD spectra was of an MCD with additional Comptonized emission (DISKBB + COMPTT in XSPEC). The free parameters of this model are the inner accretion disk temperature, disk normalization, seed photon temperature of the Comptonization, plasma temperature, plasma optical depth, and normalization of the Comptonized component. This and similar models have commonly been used to model two-component XMM-Newton spectra from more luminous ULXs (e.g., Feng & Kaaret 2009; Gladstone et al. 2009). Generally this model results in a soft MCD and hard, optically thick Comptonization. When used for ULXs the Comptonization input photon temperature is often set equal to the inner-disk temperature
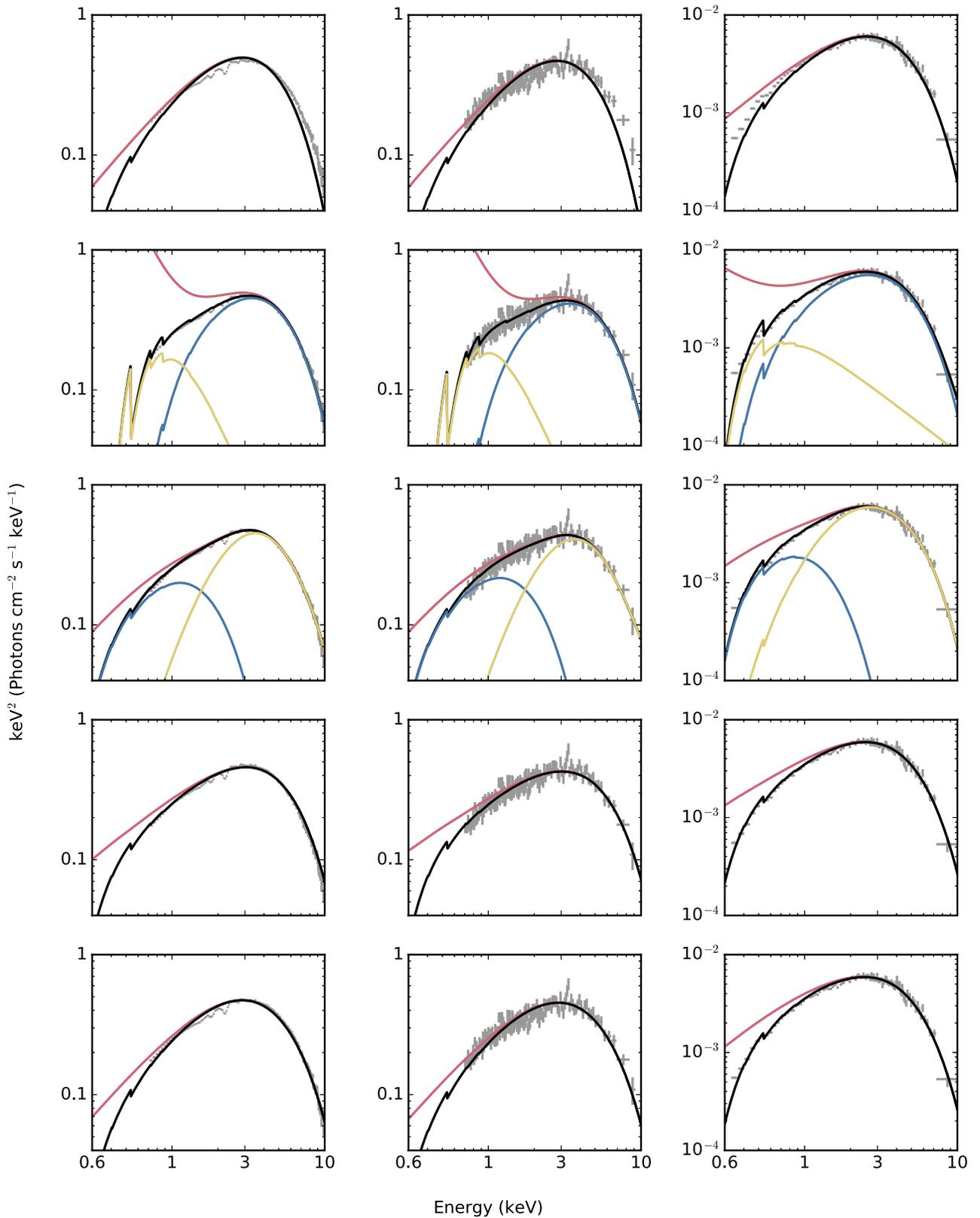
Figure 1. Examples of different spectral models fitted to TD BHB and BD ULX data. The gray data points show the real (left) and resampled (middle) spectra from LMC X-3 *XMM*-1 and the data from M31 ULX1 (right). All of the spectra have been rebinned to 10σ significance for clarity. The lines show the various models used in this work, which are (from top to bottom) an MCD, an MCD plus a power law, an MCD plus Comptonization, a *p*-free disk, and the KERRBB approximation of a thin accretion disk spectrum. Specifically, the lines show the observed model (black), the unabsorbed model (red), the MCD in two-component models (blue), and the power-law/Comptonization in two-component models (yellow). Clearly there is a large degree of degeneracy between the different spectral models.

Table 4
MCD

Source	ObsID[a]	$N_{\rm H}$[b] $(10^{22}\,{\rm cm}^{-2})$	$T_{\rm in}$[c] (keV)	$R_{\rm in}$[d] (km)	χ^2/dof[e]
		Observed BHBs			
GX 339−4	XMM-1	0.62	0.91	43	(8222.6/163)
	XMM-2	0.61	0.92	42	(3556.9/160)
LMC X-3	XMM-1	0	1.2	57	(28994.7/164)
	Swift-1	0	1.1	54	(2787.3/616)
	XMM-2	0	1.1	56	(18379.2/162)
LMC X-1	XMM-1	0.56	0.86	51	(1932.9/151)
	Swift-1	0.491 ± 0.005	0.952 ± 0.004	44	(818.2/564)
	Swift-2	0.455 ± 0.007	0.988 ± 0.006	39	(684.3/519)
		Resampled BHBs			
GX 339−4	XMM-1	0.63 ± 0.01	0.896 ± 0.008	44	593.9/559
	XMM-2	0.61 ± 0.01	0.905 ± 0.009	43	606.1/566
LMC X-3	XMM-1	[0]	1.18 ± 0.01	59	(689.2/502)
	Swift-1	[0]	1.08 ± 0.01	54	(657.1/393)
	XMM-2	[0]	1.05 ± 0.01	56	(711.1/481)
LMC X-1	XMM-1	0.57 ± 0.01	0.849 ± 0.008	51	(687.7/556)
	Swift-1	0.366 ± 0.009	0.918 ± 0.009	48	(514.0/391)
	Swift-2	$0.331^{+0.009}_{-0.008}$	0.98 ± 0.01	40	(576.9/396)
		ULXs			
M31 ULX2	…	0.296 ± 0.007	0.858 ± 0.008	>110	(528.5/309)
M31 ULX1	…	0	0.99	>93	(678.7/138)
NGC 253 XMM2	…	0.044 ± 0.004	1.16 ± 0.01	>72	(453.5/326)
NGC 253 ULX2	…	0.22 ± 0.01	1.66 ± 0.02	>46	331.9/347
M33 X-8	…	0	1.1	>84	(1849.0/163)
NGC 2403 X-1	…	$0.162^{+0.006}_{-0.005}$	1.04 ± 0.01	>100	371.3/330
NGC 4736 ULX1	…	0	0.80	>160	(608.0/241)

Notes. Parameters and fit statistics for the absorbed MCD model (TBABS × DISKBB in XSPEC) fitted to the the observed and resampled BHB spectra and the ULX spectra. Errors and limits are given to 1σ significance, and unconstrained parameters are highlighted in square brackets. Parameters are arbitrarily quoted to two significant figures for observations where the fit statistic (χ^2/dof) exceeds a value of 2. For each of the extragalactic sources an additional absorption component (TBABS) was included to account for the Galactic column density, which was fixed to the values in Tables 1 and 3.
[a] Observation identifier for the BHBs (see Table 2).
[b] Absorption column (values below 1×10^{-3} are shown as 0).
[c] Inner-disk temperature of the MCD.
[d] Approximate inner-disk radius calculated using the best-fitting model parameters and arbitrarily reported to two significant figures. It is corrected from the apparent radius using $R_{\rm in} \sim 1.19 \times r_{\rm in}$ (Kubota et al. 1998), inclinations and distances from Table 1 were assumed for the BHBs ($i \sim 25°$ was assumed for GX 339−4), and distances from Table 3 were used for the ULXs, where the lack of inclination estimates meant that only a lower limit can be given.
[e] Goodness-of-fit statistic in terms of χ^2/degrees of freedom, where values in parentheses indicate that the model can be rejected at the equivalent of $\geqslant 3\sigma$ significance.

of the MCD. This is intended as an approximation of a Comptonizing corona above an accretion disk, but fixing the temperatures in this way may not be appropriate if the corona is optically thick and obscures the inner disk from view (Gladstone et al. 2009). As such, we did not fix the Comptonization input photon temperature here. This model has also been used to fit BD ULX X-ray spectra, which has been physically interpreted as the onset of a radiatively driven wind at accretion rates close to Eddington (Middleton et al. 2011, 2012, 2013). The same model was used to fit broad, sub-Eddington accretion disk spectra from GX 339−4 when it was in the TD state (Kolehmainen et al. 2011), in which case it is a purely phenomenological model.

The parameters and fit statistics for the MCD plus Comptonization model are given in Table 6. Fits with input soft photon temperatures lower than the inner accretion disk temperature, or plasma temperatures lower than the input photon temperature, were rejected as unphysical. Similarly to

the previous model, this was not sufficient to reproduce all of the complexities in most of the complete BHB spectra, although it was sufficient for 6/8 of the resampled BHBs and 6/7 of the ULXs. Several of the the resampled TD BHB and BD ULX spectra were best fitted by optically thick coronae, although many admittedly have poorly constrained model parameters. This is reminiscent of many more luminous ULXs and is consistent with an optically thick Comptonizing corona obscuring the inner disk.

In Figure 2 we show a comparison of the DISKBB + COMPTT model parameters in the BHBs and ULXs. In general, the BHBs and ULXs tended to occupy similar regions of parameter space, with the exception of L_X. After excluding the rejected fits and the unconstrained inner-disk temperature in GX 339−1 XMM-1, we tested for rank correlations between the parameters and L_X using Kendall's τ coefficient. The resulting Kendall's τ correlation coefficients were 0.2, 0.1, 0.2, and 0.3, with p-

Table 5
MCD Plus Power Law

Source	ObsID	N_H $(10^{22} \text{ cm}^{-2})$	T_{in}[a] (keV)	Γ[b]	F_{pow}/F_{diskbb}[c]	R_{in} (km)	χ^2/dof
			Observed BHBs				
GX 339−4	XMM-1	0.92	0.90	3.2	1.4	40	(520.9/161)
	XMM-2	$0.880^{+0.010}_{-0.009}$	0.896 ± 0.002	3.03 ± 0.03	$1.23^{+0.04}_{-0.05}$	40	(289.2/158)
LMC X-3	XMM-1	0.48	1.3	4.6	5.0	46	(2325.3/162)
	Swift-1	$0.011^{+0.006}_{-0.005}$	1.178 ± 0.008	2.27 ± 0.07	0.61 ± 0.04	42	(899.2/614)
	XMM-2	0.33	1.2	3.9	3.3	40	(492.1/160)
LMC X-1	XMM-1	1.2	0.90	4.1	4.5	41	(452.5/149)
	Swift-1	$0.501^{+0.006}_{-0.005}$	$0.934^{+0.006}_{-0.010}$	-1 ± 1	$<7 \times 10^{-4}$	47	(759.0/562)
	Swift-2	$0.48^{+0.02}_{-0.01}$	$0.92^{+0.02}_{-0.01}$	$1.1^{+0.6}_{-0.9}$	<0.1	44	602.9/517
			Resampled BHBs				
GX 339−4	XMM-1	1.0 ± 0.1	0.90 ± 0.02	3.6 ± 0.4	$1.8^{+0.7}_{-0.5}$	41	579.3/557
	XMM-2	$0.80^{+0.08}_{-0.09}$	0.85 ± 0.02	$2.6^{+0.3}_{-0.4}$	$0.8^{+0.5}_{-0.3}$	44	561.6/564
LMC X-3	XMM-1	0.5 ± 0.1	$1.37^{+0.04}_{-0.03}$	$4.6^{+0.4}_{-0.5}$	6 ± 2	42	480.1/500
	Swift-1	$<9 \times 10^{-3}$	$1.164^{+0.017}_{-0.009}$	$2.2^{+0.2}_{-0.1}$	$0.50^{+0.06}_{-0.04}$	43	435.5/391
	XMM-2	[0]	$1.16^{+0.02}_{-0.03}$	$2.5^{+0.2}_{-0.1}$	3 ± 1	41	527.5/479
LMC X-1	XMM-1	1.3 ± 0.2	$0.90^{+0.01}_{-0.02}$	$4.4^{+0.7}_{-0.6}$	5 ± 2	41	623.9/554
	Swift-1	$0.8^{+0.1}_{-0.2}$	$0.94^{+0.02}_{-0.03}$	$4.7^{+0.8}_{-1.1}$	5^{+5}_{-2}	44	(503.4/389)
	Swift-2	$0.36^{+0.03}_{-0.02}$	0.91 ± 0.02	$1.5^{+0.5}_{-1.1}$	<0.3	45	(546.1/394)
			ULXs				
M31 ULX2	...	0.50 ± 0.04	$0.73^{+0.03}_{-0.02}$	2.4 ± 0.1	1.6 ± 0.4	>110	308.5/307
M31 ULX1	...	0.03 ± 0.02	1.080 ± 0.007	3.2 ± 0.2	1.01 ± 0.09	>74	179.6/136
NGC 253 XMM2	...	0.17 ± 0.02	$1.15^{+0.07}_{-0.06}$	2.1 ± 0.1	1.9 ± 0.3	>56	321.9/324
NGC 253 ULX2	...	$0.26^{+0.12}_{-0.04}$	$1.64^{+0.08}_{-0.09}$	2 ± 1	$0.3^{+0.5}_{-0.2}$	>74	(314.5/161)
NGC 2403 X-1	...	$0.45^{+0.06}_{-0.05}$	1.13 ± 0.02	$3.3^{+0.4}_{-0.3}$	2.3 ± 0.3	>79	310.2/328
NGC 4736 ULX1	...	0.10 ± 0.02	1.02 ± 0.05	2.6 ± 0.1	3.1 ± 0.4	>74	(315.3/239)

Notes. Same as Table 4, but for the absorbed MCD plus power-law model (TBABS × (DISKBB + POWERLAW) in XSPEC).
[a] Inner-disk temperature of the MCD.
[b] Power-law spectral index.
[c] Ratio of the 0.3–1 keV power-law and MCD fluxes calculated using the CFLUX convolution model in XSPEC; this is not a parameter of the model, but it is used to constrain the spectral type in the Sutton et al. (2013) ULX classification scheme.

values (for the null hypothesis of Kendall's $\tau = 0$, i.e., no correlation) of 0.5, 0.6, 0.5, and 0.2 for parameters T_{in}, T_0, kT, and τ, respectively, none of which are significant even at the 2σ level.

4.4. p-free Disk

The fourth model was of a *p*-free disk, which is an approximation of an MCD spectrum that has been modified by radial advection. This model has the parameters of the MCD model (disk temperature and normalization) plus "*p*," which is the exponent of the radial dependence of the disk temperature (i.e., $T(r) \propto r^{-p}$, where $T(r)$ is the local effective temperature at radius r). A standard MCD is recovered for $p = 0.75$, and lower values indicate a degree of advection, with $p = 0.5$ being predicted for advection-dominated disks. The model parameters and fit statistics for this model are shown in Table 7. Rather unsurprisingly, this model with only three free parameters (plus absorption) was unable to reproduce any of the real TD BHB spectra, but it was sufficient for 6/8 of the resampled BHBs and 5/7 of the ULXs. Notably, all of the best-fitting values of p were less than 0.75, indicating that advection may have been occurring in the accretion disks. Furthermore, critically, $p \geqslant 0.75$ can be ruled out at 3σ significance for all of

the BHBs and all of the ULXs except for NGC 253 ULX2. As for the previous model, we show the parameters against observed 0.3–10 keV luminosity (Figure 3). Again, we calculated the Kendall's τ coefficient to test for rank correlations between each parameter and L_X. The resulting Kendall's τ correlation coefficients were 0.6 and 0.2 with p-values of 0.02 and 0.5 for T_{in} and p, respectively. These suggest that there may be a strong rank correlation between inner-disk temperature and X-ray luminosity, although it is not highly significant (at the 3σ level), and the weighted mean inner-disk temperatures of both the BHBs and ULXs agree within the uncertainties ($\overline{T_{in}} = 1.19 \pm 0.06$ and 1.26 ± 0.05 keV for the BHBs and ULXs, respectively). In order to produce such similar temperature spectra over an order of magnitude in luminosity, the normalization, and hence the inner radius of the disk, varies between BHBs and ULXs. Given the uncertainties in inclinations and distances, only approximate values of, or limits on, the inner-disk radii can be calculated; however, these generally suggest slightly larger black holes in the ULXs. Alternatively, this could be consistent with a scenario where the accretion disk becomes strongly advective, and hence radiation trapping makes it unobservable, within a radius corresponding to a fixed temperature. Then, increases in L_X would correspond to increases in the characteristic inner-disk

Table 6
MCD Plus Comptonization

Source	ObsID	N_{H} $(10^{22}\,\mathrm{cm}^{-2})$	T_{in}[a] (keV)	T_0[b] (keV)	kT[c] (keV)	τ[d]	R_{in} (km)	χ^2/dof
				Observed BHBs				
GX 339−4	XMM-1	0.76	0.39	0.59	4.5	1.1	180	(603.9/159)
	XMM-2	0.742 ± 0.008	0.40 ± 0.01	$0.590^{+0.009}_{-0.010}$	$2.3^{+15.1}_{-0.4}$	$2.7^{+0.7}_{-2.4}$	170	(300.5/156)
LMC X-3	XMM-1	0	0.44	0.72	1.4	6.6	280	(1929.1/160)
	Swift-1	[0]	0.350 ± 0.007	$0.62^{+0.01}_{-0.02}$	$1.9^{+1.5}_{-0.3}$	4^{+1}_{-2}	320	(726.7/612)
	XMM-2	[0]	0.405 ± 0.006	0.63 ± 0.02	1.30 ± 0.04	$7.1^{+0.4}_{-0.5}$	260	(315.1/158)
LMC X-1	XMM-1	0.96	0.27	0.51	1.2	5.4	580	(351.6/147)
	Swift-1	0.65 ± 0.03	0.28 ± 0.02	0.52 ± 0.01	7^{+31}_{-6}	<3	410	(730.4/560)
	Swift-2	0.61 ± 0.04	$0.29^{+0.03}_{-0.02}$	$0.51^{+0.02}_{-0.01}$	<70	<9	340	594.8/515
				Resampled BHBs				
GX 339−4	XMM-1	$0.57^{+0.06}_{-0.05}$	$[4 \times 10^{-3}]$	0.36 ± 0.04	1.08 ± 0.03	10.8 ± 0.6	2.3×10^4	577.3/555
	XMM-2	0.8 ± 0.2	$0.23^{+0.16}_{-0.05}$	$0.41^{+0.10}_{-0.05}$	$1.2^{+0.3}_{-0.1}$	6^{+1}_{-2}	580	557.2/562
LMC X-3	XMM-1	[0]	$0.47^{+0.04}_{-0.03}$	0.80 ± 0.07	4^{+63}_{-3}	<9	260	480.1/498
	Swift-1	[0]	0.35 ± 0.02	0.63 ± 0.03	5^{+72}_{-3}	<7	320	416.7/389
	XMM-2	<0.4	$0.19^{+0.06}_{-0.05}$	$0.33^{+0.07}_{-0.11}$	$1.12^{+0.07}_{-0.05}$	10 ± 1	1.8×10^3	522.3/477
LMC X-1	XMM-1	1.03 ± 0.09	$0.25^{+0.03}_{-0.02}$	$0.50^{+0.03}_{-0.02}$	<40	<4	770	614.5/552
	Swift-1	$0.67^{+0.07}_{-0.08}$	$0.22^{+0.04}_{-0.03}$	0.46 ± 0.06	<9	6^{+2}_{-5}	1.1×10^3	(483.0/387)
	Swift-2	0.70 ± 0.06	0.21 ± 0.02	0.47 ± 0.02	50^{+20}_{-40}	<5	1.5×10^3	(509.9/392)
				ULXs				
M31 ULX2	...	0.37 ± 0.03	$0.65^{+0.13}_{-0.02}$	$1.34^{+1.44}_{-0.09}$	<100	<60	>180	312.4/305
M31 ULX1	...	$0.015^{+0.008}_{-0.010}$	$0.30^{+0.04}_{-0.03}$	$0.44^{+0.05}_{-0.03}$	<1.03	$10.7^{+0.2}_{-0.8}$	>610	176.0/134
NGC 253 XMM2	...	0.27 ± 0.03	0.07 ± 0.01	<0.2	$1.34^{+0.08}_{-0.06}$	9.0 ± 0.5	$>3.7 \times 10^4$	313.6/322
NGC 253 ULX2	...	$0.3^{+0.3}_{-0.2}$	$0.10^{+0.03}_{-0.02}$	$0.29^{+0.05}_{-0.28}$	1.41 ± 0.05	$11.2^{+0.6}_{-1.3}$	$>1.0 \times 10^4$	318.6/343
M33 X-8	...	0.047 ± 0.003	$0.48^{+0.03}_{-0.02}$	0.65 ± 0.03	<100	<3	>310	(302.0/159)
NGC 2403 X-1	...	0.26 ± 0.02	$0.41^{+0.05}_{-0.08}$	$0.72^{+0.09}_{-0.25}$	2^{+23}_{-1}	3^{+9}_{-1}	>500	303.4/326
NGC 4736 ULX1	...	[0]	0.04 ± 0.02	0.157 ± 0.007	1.05 ± 0.04	10.5 ± 0.4	$>1.2 \times 10^5$	269.1/237

Notes. Same as Table 4, but for the absorbed MCD plus Comptonization model (TBABS × (DISKBB + COMPTT) in XSPEC). Fits with hot accretion disk and cool, soft Comptonization ($T_{\mathrm{in}} > T_0$) components or low-temperature coronae ($kT < T_0$) were rejected as unphysical, and alternative local minima in χ^2 were used instead.
[a] Inner-disk temperature of the MCD.
[b] Input soft photon (Wien) temperature; this was not fixed to the inner-disk temperature.
[c] Plasma temperature; this was constrained to be >1 keV.
[d] Plasma optical depth.

radius, while the observed inner-disk temperature remains roughly constant.

Spectral shape is not the only diagnostic of an advective, slim disk. While standard disks evolve along an $L \propto T^4$ trend, slim disks are expected to follow a shallower slope (e.g., Watarai et al. 2001). There is the suggestion that the ULXs may follow a shallower trend than the BHBs in the left panel of Figure 3. However, this is not conclusive as there is no strong evidence that all of these BD ULXs have the same black hole masses or inclinations. A thorough study of this potential trend in individual sources is beyond the scope of this work.

4.5. A Thin Disk around a Kerr Black Hole

The final spectral model was of a thin accretion disk around a Kerr black hole (KERRBB in XSPEC). The free parameters of this model were black hole spin, inclination, black hole mass (fixed for the BHBs), and the effective mass accretion rate. Additional parameters that were fixed were distance from the observer; η, the torque parameter, which was set to 0; spectral hardening factor, which was set to 1.7; a flag for self-irradiation, which was fixed at 1 (i.e., included in the model);

and a flag for limb darkening, which was set to 0 (i.e., excluded from the model). Theoretically, this model is appropriate for accretion rates up to ~0.3 Eddington, above which radiation pressure begins to inflate the disk (e.g., McClintock et al. 2006) such that so-called slim-disk models with radial advection are more appropriate. In the KERRBB thin-disk model, no single parameter affects normalization alone: increasing the spin or accretion rate results in a harder spectrum and higher bolometric luminosity, while increasing the black hole mass softens the spectrum. Alternative general relativistic accretion disk models exist (see, e.g., Middleton 2015, for a summary), including BHSPEC (Davis et al. 2005). Unlike KERRBB, which assumes a constant spectral hardening factor, BHSPEC includes bound–free and free–free opacities of abundant ion species, which can produce a slightly broader spectrum (Kubota et al. 2010). However, Hui & Krolik (2008) report that there is little difference between the fits or resulting parameters when fitting KERRBB and BHSPEC to ULXs with disk-like spectra, so we only consider the KERRBB model here.

The fit statistics and parameters from the KERRBB model are given in Table 8. For the BHBs, where we are analyzing multiple observations of each source, each of the spectra were

Table 7
p-free Accretion Disk

Source	ObsID	$N_{\rm H}$ $(10^{22}\,{\rm cm}^{-2})$	$T_{\rm in}$ [a] (keV)	p [b]	$R_{\rm in}$ [c] (km)	χ^2/dof
			Observed BHBs			
GX 339−4	*XMM*-1	0.80	1.0	0.58	67	(2158.9/162)
	XMM-2	0.81	1.0	0.57	62	(1080.8/159)
LMC X-3	*XMM*-1	0	1.5	0.64	83	(3771.5/163)
	Swift-1	[0]	1.321 ± 0.008	0.642 ± 0.002	78	(920.5/615)
	XMM-2	0	1.3	0.62	75	(695.1/161)
LMC X-1	*XMM*-1	0.85	1.0	0.51	58	(581.0/150)
	Swift-1	0.53 ± 0.01	0.98 ± 0.01	0.69 ± 0.02	100	(808.1/563)
	Swift-2	0.57 ± 0.02	1.08 ± 0.02	0.62 ± 0.02	69	(649.8/518)
			Resampled BHBs			
GX 339−4	*XMM*-1	0.79 ± 0.04	0.97 ± 0.02	$0.60^{+0.03}_{-0.02}$	76	579.0/558
	XMM-2	0.83 ± 0.04	1.04 ± 0.03	0.55 ± 0.02	59	575.0/565
LMC X-3	*XMM*-1	$(9 \pm 7) \times 10^{-3}$	1.52 ± 0.04	0.613 ± 0.009	70	566.7/579
	Swift-1	[0]	1.31 ± 0.02	0.642 ± 0.005	79	441.4/392
	XMM-2	[0]	1.32 ± 0.03	$0.609^{+0.007}_{-0.006}$	69	525.5/480
LMC X-1	*XMM*-1	$0.86^{+0.03}_{-0.04}$	1.01 ± 0.03	<0.53	57	631.8/555
	Swift-1	0.47 ± 0.03	1.01 ± 0.03	$0.59^{+0.03}_{-0.02}$	79	(499.3/390)
	Swift-2	0.45 ± 0.02	$1.13^{+0.04}_{-0.03}$	0.57 ± 0.02	57	(551.6/395)
			ULXs			
M31 ULX2	…	$0.527^{+0.006}_{-0.007}$	1.18 ± 0.02	<0.502	>81	351.6/308
M31 ULX1	…	$<2 \times 10^{-3}$	1.139 ± 0.009	$0.664^{+0.002}_{-0.004}$	>160	(194.9/137)
NGC 253 XMM2	…	0.15 ± 0.01	$1.57^{+0.06}_{-0.05}$	0.576 ± 0.009	>72	326.0/325
NGC 253 ULX2	…	0.25 ± 0.02	1.75 ± 0.05	0.70 ± 0.02	>100	327.5/346
M33 X-8	…	0.099	1.4	0.58	>90	(470.7/162)
NGC 2403 X-1	…	0.28 ± 0.02	$1.25^{+0.04}_{-0.03}$	0.59 ± 0.01	>140	312.5/329
NGC 4736 ULX1	…	0.054 ± 0.009	$1.31^{+0.06}_{-0.05}$	$0.537^{+0.010}_{-0.009}$	>92	294.9/240

Notes. Same as Table 4, but for the absorbed *p*-free disk model (TBABS × DISKPBB in XSPEC).
[a] Inner-disk temperature of the *p*-free disk in keV.
[b] Exponent of the radial dependence of the disk temperature.
[c] The inner-disk radius is corrected from the apparent radius using $R_{\rm in} \sim 3.19 \times r_{\rm in}$ (Vierdayanti et al. 2008).

fitted simultaneously with spin and inclination fixed between them. The model can be rejected for all of the real BHB data sets, and it is only acceptable in 1/3 of the resampled BHBs and 3/7 of the ULXs. When fitting the BHBs, we fixed the black hole mass to the values given in Table 1. As an additional test, we refitted both the real and resampled spectra from GX 339−4 while allowing the black hole mass to vary within the quoted uncertainty range. For the real data, the improvement in the fit statistic was marginally significant based on an *f*-test (at the 2σ level, but not the 3σ level), although the model could still be strongly rejected (χ^2/dof = 3564.4/322). Despite the slight improvement in fit, allowing the black hole mass to vary did not result in large changes ($\lesssim$10%) to the other model parameters. No such improvement in fit was found for the resampled data ($\Delta\chi^2 = -0.9$ for 1 fewer degree of freedom), and the model parameters were consistent within the 1σ uncertainty regions with those from the fixed-mass model.

Although some of the model parameters appear to be very precise, we would caution against assuming them to be accurate, especially given the degeneracies between model parameters and the questionable physical basis of using a thin-disk model. Additionally, when using spectral continuum fitting to determine meaningful estimates of the black hole spin, it is necessary to fix the inclination, mass, and distance to known values (e.g., McClintock et al. 2014). We do not fix the inclination here, as it is not currently feasible in the ULXs, and measuring spin is not the purpose of this paper. Despite this, we note that the model results in spin and inclination estimates for GX 339−4 and LMC X-1 (from the resampled spectra) that agree with at least some reported results (although these are not always in consensus with each other, or particularly well constrained), while for LMC X-3, our values disagree with the literature: GX 339−4—$a \approx 0.93$ (Miller et al. 2008), $a > 0.97$ (Ludlam et al. 2015), $a < 0.9$ (Kolehmainen & Done 2010), $i = 20°$–$30°$ (Miller et al. 2004; Reis et al. 2008; Plant et al. 2014), $i > 45°$ (Kolehmainen & Done 2010); LMC X-3—$a \approx 0.21$ (Steiner et al. 2014), $i \approx 70°$ (Orosz et al. 2014); LMC X-1—$a \approx 0.92$ (Gou et al. 2009), $i \approx 36°$ (Orosz et al. 2009). The disagreement in the case of LMC X-3 is hardly surprising, given that the spectral model was strongly rejected. While the range of parameters for the previous models did not vary significantly between the TD BHBs and BD ULXs, except for luminosity, this is not the case here. The fitted black hole masses in the ULXs varied in the range of ∼40–80 $M_\odot$, while values from Table 1 were used for the BHBs. Additionally, the black hole spins were relatively poorly constrained in the BHBs, but close to maximal in the ULXs, and mass accretion rates were significantly higher in the ULXs too. Despite the
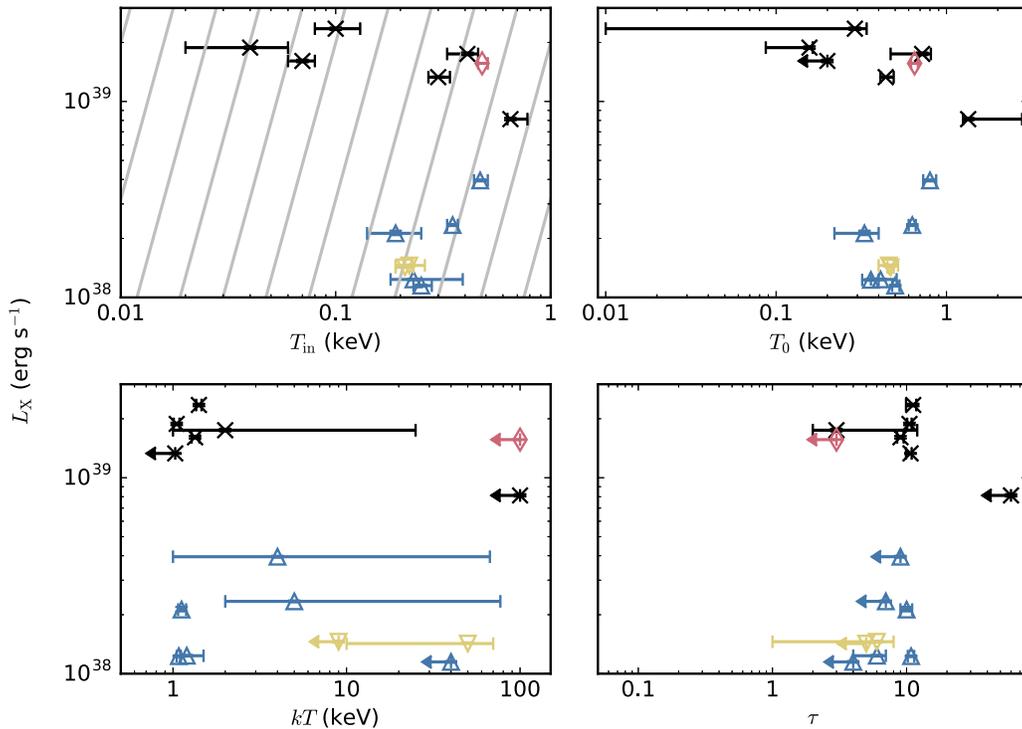
Figure 2. Parameters of the absorbed MCD plus Comptonization spectral model plotted against the observed 0.3–10 keV luminosity estimated from the same model. The symbols correspond to ULXs where the model is statistically acceptable (at 3σ significance; black crosses), ULXs where the model is rejected (red diamonds), BHBs where the model is acceptable (blue upward-pointing triangles), and BHBs where the model is rejected (yellow downward-pointing triangles). Reading across the rows from top left, the model parameters shown are the inner-disk temperature of the MCD, the input soft photon temperature, the plasma temperature, and the plasma optical depth. The gray lines in the top left panel show arbitrary $L \propto T^4$ relations as would be appropriate for a thin accretion disk. No significant correlations were found between the model parameters and luminosity.

differences in parameters, the approximate Eddington ratios of the BHBs and ULXs largely overlapped with both classes, typically falling between ~ 0.1 and 0.4. The sole exception to this was NGC 253 ULX2, which had a higher Eddington ratio of ~ 0.9, but we note that the black hole mass parameter could not be constrained by the data, so this estimate is subject to extremely large uncertainties.

Overall, the KERRBB parameters suggested that the ULXs contained slightly larger black hole primaries than the BHBs, and they were at close to maximal spin. However, the KERRBB model is rejected in four out of the seven ULXs, so the variables of the model cannot necessarily be simply interpreted as the physical parameters of the ULX binary systems. Indeed, in the case of M31 ULX2, the black hole mass is clearly in disagreement with the constraints from luminosity limits based on a sub-Eddington spectral state when it is faint ($<17 \, M_\odot$; Middleton et al. 2013). Fixing the black hole to $10 \, M_\odot$ for this source resulted in a significantly worse fit statistic ($\chi^2/\mathrm{dof} = 469.9/308$ or $\Delta\chi^2 = 49.3$ for 1 additional degree of freedom) compared to the model with the black hole mass free to vary (which had a black hole mass of $46^{+6}_{-2} \, M_\odot$, where the uncertainties are reported at the 1σ level), with a corresponding f-test probability of 5.6×10^{-9}. Additionally, fixing the black hole mass resulted in the model having retrograde spin ($a = -0.8 \pm 0.2$; see Middleton et al. 2014) and a significantly higher mass accretion rate ($M_{\mathrm{dd}} = 28^{+6}_{-5} \times 10^{18} \, \mathrm{g \, s^{-1}}$, or $l \sim 2$). This may not be surprising since black hole accretion disks are not expected to remain geometrically thin as $l \to 1$.

4.5.1. Additional Power Law Emission

Although we attempted to exclude spectra with obvious high-energy power-law emission, it was evident from the spectral residuals from the KERRBB model fitted to the real BHB spectra that some may deviate from pure disk spectra (Figure 4). However, in the BHB with the largest deviation between the model and data, GX 339−4, the KERRBB model was able to adequately fit the $\sim 25{,}000$-count resampled spectra. This indicates that relatively weak power-law emission (as in the TD state) may not be detected if present in similar-quality observations of nearby ULXs. Regardless of this, we added a power-law component to the KERRBB model using the SIMPL convolution model in XSPEC and tested whether this improved the fits to the real BHB spectra (Table 9). The SIMPL model has parameters of spectral index, the fraction of the input emission that is reprocessed into the power law, and a flag for up-scattering only, or both up- and down-scattering, which was set to up-scattering only. Indeed, adding this component resulted in large improvements in the fit statistic: $\Delta\chi^2 = -2340.8, -1912.8,$ and -794.1, for 4, 6, and 6 fewer degrees of freedom, in GX 339−4, LMC X-3, and LMC X-1, respectively, although all of these fits were still rejected at 3σ significance.

As with the previous model, we used the real and resampled spectra from GX 339−4 to test whether allowing the black hole mass to vary within the range given in Table 1 significantly altered the fits. No significant improvements in the fit statistics were found (at the $>95\%$ level, based on an f-test), and the model parameters did not vary significantly from the fixed-mass model
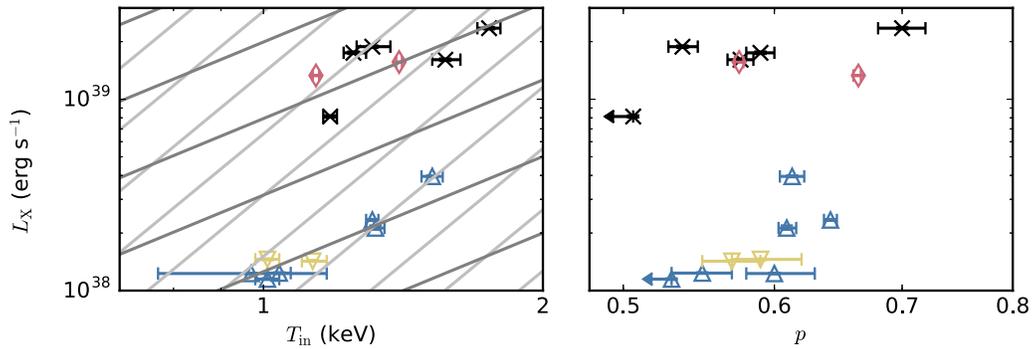
Figure 3. Same as Figure 2, but for the parameters of the *p*-free disk model. The left panel shows the inner-disk temperature, where the gray lines show characteristic luminosity–temperature relations with arbitrary normalizations. The light-gray lines correspond to $L \propto T^4$, which is the standard relation for thin accretion disks, and the dark-gray lines show $L \propto T^2$, which may be appropriate for the slim-disk regime (Kubota & Makishima 2004). The right panel shows the *p*-value. Although there is a potential correlation between luminosity and disk temperature, this is not highly significant (at the 3σ level).

(they were within the 1σ uncertainty regions where calculated, or varied by <10%).

For both observations of GX 339−4 only ∼2% of the model intrinsic disk flux was emitted as a power law, which had a spectral index of ∼1–2 (although a higher scattering fraction and softer spectral index were found for the subsampled data). These values are consistent with fits to sources in the TD state (see Steiner et al. 2009). We generally found extremely soft power law spectral indices in LMC X-3 and X-1, with large fractions of the input intrinsic disk flux being scattered ($\Gamma \sim 4.5$ and scattered fraction $f_{\rm sc} \sim 0.3$–0.6; LMC X-1 *Swift*-1 had a very hard power law, resulting in a large fraction of the intrinsic model disk flux being scattered out of the 0.3–10 keV band, but this was not well constrained), and as such we caution against interpreting these physically. Nevertheless, if we do attempt to interpret them physically, they may suggest that LMC X-3 and LMC X-1 during the *Swift* observations were in a steep power-law (see Steiner et al. 2009) or possibly hypersoft (Uttley & Klein-Wolt 2015) state. However, an inspection of the hard residuals to LMC X-3 indicated that the SIMPL power law was not a good fit to the data (Figure 4), so it may not be possible to trivially interpret this as a physical component. Additionally, LMC X-3 has previously nearly always been observed with a TD spectrum (e.g., Steiner et al. 2010). As such, we do not rule out a TD spectrum in this source. On the other hand, LMC X-1 has previously been seen with both TD and steep power-law spectra (e.g., Alam et al. 2014), and, for the *Swift* observations, the SIMPL power law eliminated the residuals above ∼5 keV. It is possible that LMC X-1 was in the steep power-law state during the *Swift* observations, and thus not dominated by emission from the accretion disk in the 0.3–10 keV energy range. When we eliminated these observations and only fitted LMC X-1 *XMM*-1, the KERRBB model was marginally acceptable at the 3σ level for the resampled data ($\chi^2/{\rm dof} = 651.6/555$, corresponding to a null hypothesis likelihood of 0.997), although broad-disk and two-component models had fit statistics that were lower still.

We also tested whether modifying the ULX KERRBB fits with the SIMPL convolution model could improve the fits (Table 9). This additional component resulted in improvements in the fit statistic of $\Delta\chi^2 = -112.1, 0, -409.5$, and -81.4 for 2 fewer degrees of freedom, for M31 ULX2, M31 ULX1, M33 X-8, and NGC 4736 ULX1, respectively, where the KERRBB alone was rejected. Notably, this model resulted in a statistically acceptable fit for M31 ULX2 ($\chi^2/{\rm dof} = 308.5/305$), where the parameters indicated a ∼70 $M_\odot$ black hole in the TD state with only ∼0.7%

of the intrinsic disk flux being reprocessed into a hard ($\Gamma \sim 1.4$) power law. Also, the SIMPL model parameters indicated that M33 X-8 and NGC 4736 ULX1 may have spectra similar to steep power-law state BHBs ($\Gamma \approx 2.9$, $f_{\rm sc} \approx 0.3$ and $\Gamma \approx 3.1$, $f_{\rm sc} \approx 0.6$ respectively); however, these fits were still rejected at >3σ significance ($\chi^2/{\rm dof} = 312.7/159$ and $326.1/237$), indicating that the BD spectra in these ULXs are unlikely to be due to an unresolved hard power-law component.

4.6. Additional Emission Components in M33 X-8

While most of the ULXs could be well fitted by at least some of the spectral models, no statistically acceptable model was found for M33 X-8. This could potentially indicate that additional spectral emission components were present in this source. Indeed, La Parola et al. (2003) reported a broad Gaussian emission line at ∼0.9 and ∼0.2 keV thermal emission from a hot plasma in the *Chandra* ACIS spectrum of M33 X-8, and Owen & Warwick (2010) reported that extended emission in the galaxy could be fitted by a dual thermal plasma spectrum, with $kT \sim 0.2$ and 0.6 keV. The addition of a broad Gaussian emission line resulted in the fit statistic being improved by $\Delta\chi^2 = -115.2, -58.4, -80.7$, and -308.1 for 3 fewer degrees of freedom, for the MCD plus power-law, MCD plus Comptonized emission, *p*-free disk, and KERRBB models, respectively. However, the parameters of the emission line were dependent on the continuum model. For the first three models the line energy and width were $E \sim 1.1$ keV and $\sigma \sim 0.2$ keV, while for the KERRBB model they were $E \sim 0.8$ keV and $\sigma \sim 0.5$ keV. An additional ∼0.2 keV mekal plasma component did not further improve any of the fits.

4.7. X-ray Timing

We have been fitting the BHB and ULX spectra with physical and phenomenological models of emission from accretion disks. As a further test of whether single-component spectral models were appropriate for the ULXs, we examined their timing properties by extracting fractional normalized covariance spectra. We were able to constrain the fractional variability in one energy bin, and thus could extract covariance, for two of the ULXs (NGC 253 XMM2 and NGC 4736 ULX1) and three of the BHB observations (GX 339−4 *XMM*-1, *XMM*-2, and LMC X-3 *XMM*-1). The resulting fractional normalized covariance spectra are shown in Figures 5 and 6. Constant fractional normalized covariance could not be strongly ruled

Table 8
A Thin Accretion Disk around a Kerr Black Hole

Source	ObsID	N_H $(10^{22}\,cm^{-2})$	a [a]	i [b] (deg)	M_{BH} [c] $(M_\odot)$	$\dot{M}_{eff}$ [d] $(10^{18}\,g\,s^{-1})$	l [e]	χ^2/dof
			Observed BHBs					
GX 339−4	XMM-1	0.69	0.35	57	7.5	3.1	0.21	(3656.0/323)
	XMM-2	0.68	…	…	…	3.1	0.21	…
LMC X-3	XMM-1	0	0.80	48	7.0	3.4	0.41	(20997.7/943)
	Swift-1	0	…	…	…	1.9	0.23	…
	XMM-2	0	…	…	…	1.9	0.23	…
LMC X-1	XMM-1	0.61	0.64	56	10.9	2.2	0.14	(3088.1/1235)
	Swift-1	0.60	…	…	…	2.7	0.16	…
	Swift-2	0.61	…	…	…	2.5	0.15	…
			Resampled BHBs					
GX 339−4	XMM-1	0.69 ± 0.01	$0.4^{+0.1}_{-0.3}$	53^{+17}_{-7}	7.5	3^{+2}_{-1}	0.21	1158.4/1125
	XMM-2	0.68 ± 0.01	…	…	…	3^{+2}_{-1}	0.21	…
LMC X-3	XMM-1	[0]	$0.80^{+0.08}_{-0.02}$	48 ± 1	7.0	3.3 ± 0.1	0.39	(1714.3/1377)
	Swift-1	[0]	…	…	…	1.92 ± 0.08	0.23	…
	XMM-2	[0]	…	…	…	$1.83^{+0.08}_{-0.07}$	0.22	…
LMC X-1	XMM-1	0.57 ± 0.01	$0.94^{+0.05}_{-0.50}$	38^{+31}_{-8}	10.9	$1.1^{+3.1}_{-0.3}$	0.13	(1781.8/1344)
	Swift-1	0.58 ± 0.01	…	…	…	$1.3^{+3.7}_{-0.3}$	0.15	…
	Swift-2	0.61 ± 0.01	…	…	…	$1.3^{+3.5}_{-0.3}$	0.14	…
			ULXs					
M31 ULX2	…	$0.345^{+0.007}_{-0.013}$	$0.990^{+0.009}_{-0.011}$	47^{+1}_{-2}	46^{+6}_{-2}	$5.0^{+0.4}_{-1.0}$	0.20	(420.6/307)
M31 ULX1	…	0	>0.9995	64 ± 1	80 ± 4	$4.67^{+0.24}_{-0.02}$	0.15	(240.6/136)
NGC 253 XMM2	…	0.071 ± 0.004	>0.98	57^{+2}_{-6}	42^{+2}_{-9}	$6.6^{+1.5}_{-0.4}$	0.33	357.3/324
NGC 253 ULX2	…	0.22 ± 0.02	$0.91^{+0.06}_{-0.29}$	>80	[50]	40^{+50}_{-20}	0.89	325.4/345
M33 X-8	…	0.026	1.0	53	42	6.6	0.33	(720.2/161)
NGC 2403 X-1	…	0.204 ± 0.006	>0.97	57 ± 4	70^{+10}_{-20}	7^{+4}_{-2}	0.26	320.8/328
NGC 4736 ULX1	…	[0]	>0.989	57^{+1}_{-15}	88^{+8}_{-36}	$7.5^{+0.8}_{-0.3}$	0.18	(400.3/239)

Notes. Same as Table 4, but for the absorbed KERRBB model (TBABS × KERRBB in XSPEC). For the BHBs the model was fitted to all observations simultaneously. The absorption column and accretion rate were allowed to vary between observations of a single source, but the black hole mass, spin, and inclination were fixed between epochs and are shown for only the first observation of each source.
[a] Black hole spin.
[b] Disk inclination.
[c] Black hole mass; for the BHBs this was fixed to the value, or the value in the middle of the range, given in Table 1.
[d] Effective mass accretion rate.
[e] Approximate Eddington ratio calculated as $\eta M_{dd} c^2 / (M_{BH} \times 1.3 \times 10^{38}\,erg\,s^{-1}\,M_\odot^{-1})$, where η is the standard radiative efficiency of a black hole, which was calculated for each source using the best-fitting value of the spin parameter shown here (note that Eddington ratio is not a parameter of the model).

out for any of the ULXs ($\chi^2/dof = 1.6/2$ and $3.4/1$ for NGC 253 XMM2 and NGC 4736 ULX1, respectively, when fitted with a constant), albeit with the caveat that covariance could only be extracted from two of the ULXs, and even for these several values were admittedly poorly constrained. We note that Middleton et al. (2012) reported fractional covariance in M31 ULX1 that varied with energy, but for different energy and temporal binning schemes than we used here. For the BHBs, a constant value of fractional normalized covariance could be rejected at 3σ significance in a single observation: XMM-1 of GX 339−4 ($\chi^2/dof = 31.8/4$). Constant values were not rejected at 3σ significance in GX 339−4 XMM-2 or LMC X-3 XMM-1 ($\chi^2/dof = 9.5/4$ and $13.5/4$, respectively).

The covariance spectra from observation XMM-1 of GX 339−4 peaked in the hard band, as would be expected if a hard, variable power law was contributing to the energy spectrum. We tested whether the covariance spectrum from this observation was consistent with the shape of the hard power

law in the SIMPL∗KERRBB model. We converted the (nonfractional) normalized covariance spectra to XSPEC spectra using FLX2XSP and fitted it with the SIMPL power law.[13] An additional constant was added to the model to allow the normalization to vary, while all other model parameters were fixed to the best-fitting values from the spectral fitting. The resulting fit statistic was $\chi^2/dof = 7.9/4$, which cannot be rejected even at 2σ significance.

5. Discussion

We have fitted the energy spectra of sub-Eddington ($l \gtrsim 0.1$) BHBs in the 0.3–10 keV energy range with accretion disk

---

[13] To isolate the power law from the convolution model, we added an additional KERRBB component, i.e., TBABS × TBABS × (SIMPL ∗ KERRBB + KERRBB), with all parameters except normalization equal in both of the accretion disk components. The normalization of the second KERRBB component was set equal to $f_{sc} - 1$.
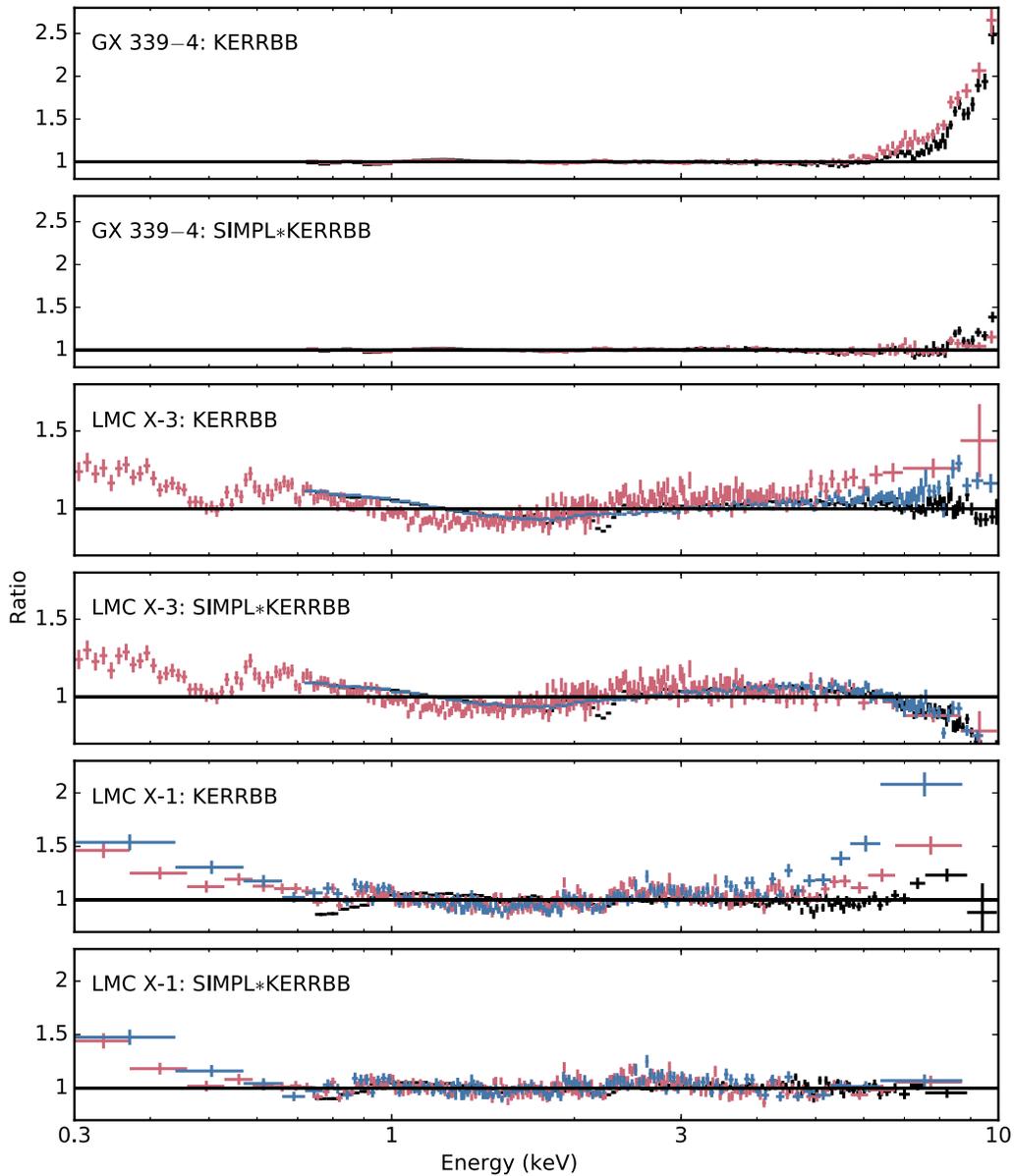
Figure 4. Residuals to the best-fitting absorbed KERRBB and SIMPL ∗ KERRBB models for the real BHB data plotted as ratios. Colors correspond to the different observations, with black being the first, red the second, and blue the third observation in order of observation date as given in Table 2. The data have been rebinned to 20σ significance for clarity. It was evident that the absorbed KERRBB model alone underpredicted the 5–10 keV flux in most of the BHB spectra, which may indicate the presence of a power-law-like tail, even in the *XMM-Newton* and *Swift* energy band. For GX 339−4 and LMC X-1 the addition of a SIMPL power-law component reduced the hard residuals. The model parameters indicated that GX 339−4 and LMC X-1 *XMM*-1 were in the TD state, while LMC X-1 *Swift*-1 and *Swift*-2 may have steep power-law spectra. However, for LMC X-3 the combination of a thin disk and SIMPL power-law spectrum resulted in large negative residuals at high energies, bringing the validity of the model into question.

emission models. The models were for the most part insufficient to reproduce the spectra from the BHBs unless they were subsampled to be comparable to the ULX sample. However, it was clear that many of the BHB spectra, even at these low Eddington ratios, were broader than expected from standard geometrically thin, optically thick disks, i.e., from a purely thermal MCD disk model. This is evident in the example of LMC X-3 *XMM*-1 (Figure 7) and in the spectral residuals when LMC X-3 and X-1 are fitted with the KERRBB model (Figure 4). In GX 339−4 some of this broadening is probably due to a hard power-law component; however, there is no strong evidence of this in any other object. In fact, the fit statistic improved significantly in other sources when a power law or Comptonization component was added to the spectral

model, but we interpret this strictly phenomenologically as a means of broadening the model spectrum rather than as a true second spectral component. A similar conclusion was reached recently by Kolehmainen et al. (2011) for GX 339−4.

More importantly, the spectral shape of our sample of BD ULXs could not be significantly distinguished from the BHBs in this study. This is rather interesting as it potentially weakens arguments for the BD and TD sources being in physically distinct states. Theoretically, the standard thin disk is expected to transition to a slim accretion disk state at high luminosities, where radiation pressure causes the scale height of the disk to increase and advection of radiation to alter the emissivity structure of the disk. Such advection-dominated disks have spectra that are broader and less peaked than standard

Table 9
A Thin Accretion Disk around a Kerr Black Hole Plus a Power Law

Source	ObsID	$N_{\rm H}$ (10^{22} cm^{-2})	Γ[a]	$f_{\rm sc}$[b]	a	i (deg)	$M_{\rm BH}$ ($M_\odot$)	$M_{\rm dd}$ (10^{18} g s^{-1})	l	χ^2/dof	$\Delta\chi^2/\Delta$dof[c]
					Observed BHBs						
GX 339−4	*XMM*-1	0.69	1.1	0.016	0.38	53	7.5	2.9	0.20	(1315.2/319)	−2340.8/4
	XMM-2	0.69	2.3	0.025	...	...	...	2.8	0.19	...	...
LMC X-3	*XMM*-1	0	4.5	0.42	0.65	45	7.0	3.6	0.34	(19085.0/937)	−1912.8/6
	Swift-1	0	4.5	0.57	...	...	...	2.0	0.19	...	...
	XMM-2	0	4.5	0.39	...	...	...	2.0	0.19	...	...
LMC X-1	*XMM*-1	$0.648^{+0.002}_{-0.005}$	4.5 ± 0.4	$0.12^{+0.04}_{-0.02}$	$0.44^{+0.04}_{-0.08}$	58^{+3}_{-2}	10.9	$2.9^{+0.4}_{-0.2}$	0.14	(2294.0/1229)	−794.1/6
	Swift-1	$0.548^{+0.002}_{-0.003}$	[1]	$0.4552^{+0.0128}_{-0.0004}$	...	...	...	$6.0^{+1.1}_{-0.2}$	0.30	...	...
	Swift-2	0.544 ± 0.006	$4.48^{+0.21}_{-0.03}$	$0.606^{+0.070}_{-0.006}$	...	...	...	$2.6^{+0.4}_{-0.2}$	0.13	...	...
					Resampled BHBs						
GX 339−4	*XMM*-1	0.692 ± 0.007	[1]	$0.267^{+0.176}_{-0.005}$	$0.35^{+0.02}_{-0.23}$	47.7 ± 0.4	7.5	$3.67^{+4.48}_{-0.02}$	0.24	1142.1/1121	−16.3/4
	XMM-2	0.701 ± 0.007	$3.7^{+0.2}_{-2.6}$	0.14 ± 0.01	...	...	...	$2.58^{+1.41}_{-0.02}$	0.17	...	...
LMC X-3	*XMM*-1	0	$3.52^{+0.08}_{-0.09}$	$0.61^{+0.14}_{-0.02}$	$0.367^{+0.007}_{-0.102}$	44.5 ± 0.3	7.0	3.87 ± 0.03	0.28	(1644.0/1371)	−70.3/6
	Swift-1	0	4.16 ± 0.07	[1]	...	...	...	$2.15^{+1.75}_{-0.02}$	0.16	...	...
	XMM-2	0	$4.23^{+).09}_{-0.08}$	$0.8^{+0.1}_{-0.2}$	...	...	...	$2.14^{+0.32}_{-0.02}$	0.15	...	...
LMC X-1	*XMM*-1	$0.633^{+0.007}_{-0.008}$	$1.3^{+0.5}_{-0.3}$	$0.013^{+0.002}_{-0.004}$	$0.926^{+0.003}_{-0.002}$	$31.1^{+9.7}_{-0.8}$	10.9	$1.183^{+0.007}_{-0.016}$	0.13	(1676.0/1338)	−105.8/6
	Swift-1	$0.605^{+0.007}_{-0.008}$	$4.5^{+0.5}_{-0.1}$	$0.22^{+0.01}_{-0.02}$	...	...	...	$1.31^{+0.29}_{-0.01}$	0.14	...	...
	Swift-2	$0.560^{+0.007}_{-0.008}$	$4.6^{+0.2}_{-0.1}$	0.56 ± 0.02	...	...	...	$1.076^{+0.018}_{-0.006}$	0.12	...	...
					ULXs						
M31 ULX2	...	0.40 ± 0.02	$2.6^{+0.7}_{-1.3}$	$0.2^{+0.7}_{-0.1}$	>0.5	[42]	>30	5^{+66}_{-1}	0.13	308.5/305	−112.1/2
M31 ULX1	...	[0]	[45]	[3 × 10^{-19}]	>0.9995	64 ± 1	81^{+3}_{-4}	$4.66^{+0.24}_{-0.02}$	0.15	(240.6/134)	0.0/3
NGC 253 XMM2	...	$0.089^{+0.003}_{-0.006}$	$3.24^{+0.26}_{-0.04}$	>0.5	$0.9949^{+0.0006}_{-0.1066}$	$57.7^{+0.5}_{-12.3}$	101^{+69}_{-2}	5^{+12}_{-1}	0.09	325.9/322	−31.4/2
NGC 253 ULX2	...	0.22 ± 0.01	[1]	<0.09	0.91 ± 0.06	>80	50^{+40}_{-20}	40^{+40}_{-20}	0.90	325.3/343	−0.1/2
M33 X-8	...	$0.042^{+0.002}_{-0.001}$	$3.4^{+0.2}_{-0.4}$	>0.3	>0.5	57^{+2}_{-4}	80 ± 10	$5.3^{+1.4}_{-0.9}$	0.13	(310.7/159)	−409.5/2
NGC 2403 X-1	...	0.207 ± 0.004	$1.03^{+3.84}_{-0.03}$	$0.049^{+0.025}_{-0.007}$	>0.98	$57.8^{+0.4}_{-5.0}$	78 ± 1	$7.64^{+1.44}_{-0.05}$	0.25	319.8/326	−1.0/2
NGC 4736 ULX1	...	0	$3.23^{+0.14}_{-0.04}$	[1]	$0.9962^{+0.0004}_{-0.0323}$	$53.2^{+0.7}_{-6.0}$	188^{+62}_{-5}	$4.7^{+18.5}_{-0.8}$	0.052	(318.9/237)	−81.4/2

Notes. Same as Table 8, but with an additional power-law component (TBABS × SIMPL ∗ KERRBB in XSPEC). The parameters of the SIMPL power law were allowed to vary between observations of a single source.
[a] Power-law spectral index.
[b] Fraction of the intrinsic disk flux that is scattered into the power law.
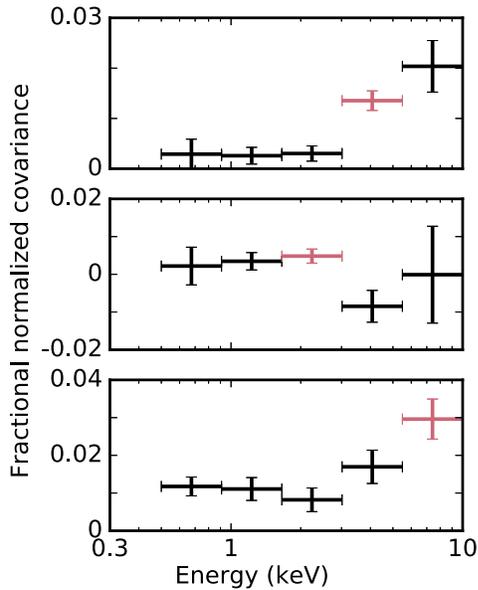[c] Improvement in the fit statistic relative to the absorbed KERRBB model alone.

Figure 5. Fractional normalized covariance spectra of GX 339−4 *XMM*-1 (top), *XMM*-2 (middle), and LMC X-3 *XMM*-1 (bottom). Red data points correspond to reference bands, where fractional rms variability is plotted instead. Constant fracitonal normalized covariance can be rejected at 3σ significance in GX 339−4 *XMM*-1, indicating the presence of a second spectral component.
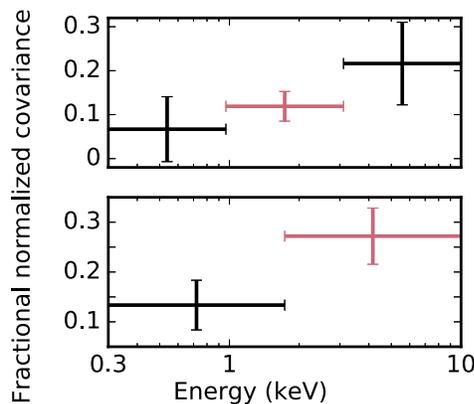

Figure 6. Fractional normalized covariance spectra of NGC 253 XMM2 (top) and NGC 4736 ULX1 (bottom). Red data points correspond to reference bands, where fractional rms variability is plotted instead. Both of the sources were consistent (at 3σ significance) with having constant fractional normalized covariance, thus there is no strong requirement for two-component models.

geometrically thin disks (for more detailed discussions of slim disks see, e.g., Abramowicz et al. 1988; Sądowski 2009). Indeed, the *p*-free disk approximation of an advection-dominated disk was sufficient to reproduce most of the BD ULX and the resampled BHB spectra. However, accretion disks are only thought to become sufficiently radiation pressure dominated to enter the slim-disk regime above $l \sim 0.3$ (McClintock et al. 2006; Steiner et al. 2010; Straub et al. 2011), whereas the BHB spectra appear to be broadened at values as low as $l \sim 0.1$. We note that spectral shape is not the only difference between thin and slim disks, and a further test of the nature of these accretion disks could come from the luminosity–temperature relation. Standard thin accretion disks follow $L \propto T^4$, while the luminosity of a slim disk would increase less steeply with temperature ($L \propto T^2$; Kubota & Makishima 2004). However, to avoid degeneracies with black

hole masses and inclinations, this is best studied in individual objects, so it is beyond the scope of this work.

As BD-like spectra are seen at low Eddington ratios, such spectra cannot be considered as a unique signature of approximately Eddington rate accretion as we had anticipated. Therefore, it is not clear how to estimate the innermost stable circular orbit (and hence constrain the compact object mass) from the normalization of the disk models, as different coefficients are often used for standard (Shimura & Takahara 1995; Kubota et al. 1998; Davis et al. 2005) and slim regimes (Vierdayanti et al. 2008), perhaps with some continuous range in between. Despite this, given the similar spectra of the BHB and BD ULX sources, it is tempting to speculate whether they may all be at similar Eddington ratios, $l \sim 0.1$–0.4. Theoretically, the most physically representative model of this state applied in this work is the KERRBB model. Although this model is statistically ruled out for four of the seven ULX observations, this is also the case in two of the three subsampled BHBs, which have known Eddington ratios of $l \approx 0.1$–0.4. The KERRBB model parameters suggest that the BD ULXs contain unusually massive black hole primaries ($\sim$40–90 $M_\odot$) with close to maximal spin (see Hui & Krolik 2008). To put this into context, the recent first gravitational wave detection was from the merger of two black holes in a binary with similarly large masses of $\sim$29 and 36 $M_\odot$, but with lower initial spin ($a < 0.7$ at least for the higher-mass primary (Abbott et al. 2016). It is possible that the intrinsic disk spectra that we study here are inherently broader than the models that we use, such that the KERRBB fits overestimate spin, as this gives larger relativistic broadening.

There are several problems with strict acceptance of the parameter values (besides the poor fit statistics) that we obtain for the ULXs from the KERRBB model. First, the black hole masses implied for many of these ULXs fall into the "second mass gap" predicted for compact object evolution. This mass gap covers the range of $\sim$60–130 $M_\odot$ over which it is thought that stellar black holes do not form due to disruption by pair instability supernovae (Marchant et al. 2016). Furthermore, black holes below the mass gap may be limited to $<$50 $M_\odot$ by severe mass loss in pulsation pair instability supernovae (Belczynski et al. 2016). Also, the collapse of massive stars is only thought to produce black hole spins of $a < 0.75$–0.9 (Gammie et al. 2004). Stellar remnant black holes undergoing Roche lobe overflow could be spun up (Podsiadlowski et al. 2003; Fragos & McClintock 2015), but to achieve maximal spin, an initially nonspinning black hole must have accreted $\gtrsim$75% of its current mass (Bardeen 1970; King & Kolb 1999). For a present-day 50 $M_\odot$ black hole to accrete $>$37 $M_\odot$ would take $\sim$5 × 10^8 yr at a constant rate of 5 × 10^{18} g s^{-1}. This is much greater than the $\lesssim$10^7 yr life span of the required donor star. Finally, if the BD ULXs contain systematically larger black holes than those seen in Galactic binaries, yet all are accreting at sub-Eddington rates, then it would be unlikely that BD ULXs could almost exclusively bridge the gap in X-ray luminosity between the BHBs at $L_X < 10^{39}$ erg s^{-1} and the two-component ULXs typically seen at $L_X > 3 \times 10^{39}$ erg s^{-1} (Sutton et al. 2013). If the BD ULXs are sub-Eddington and the two-component ULXs are at $l > 1$, then there is a missing population of sources at $l \sim 1$.

We note that the combination of high accretor mass and high spin in the KERRBB model is necessary to maintain a high
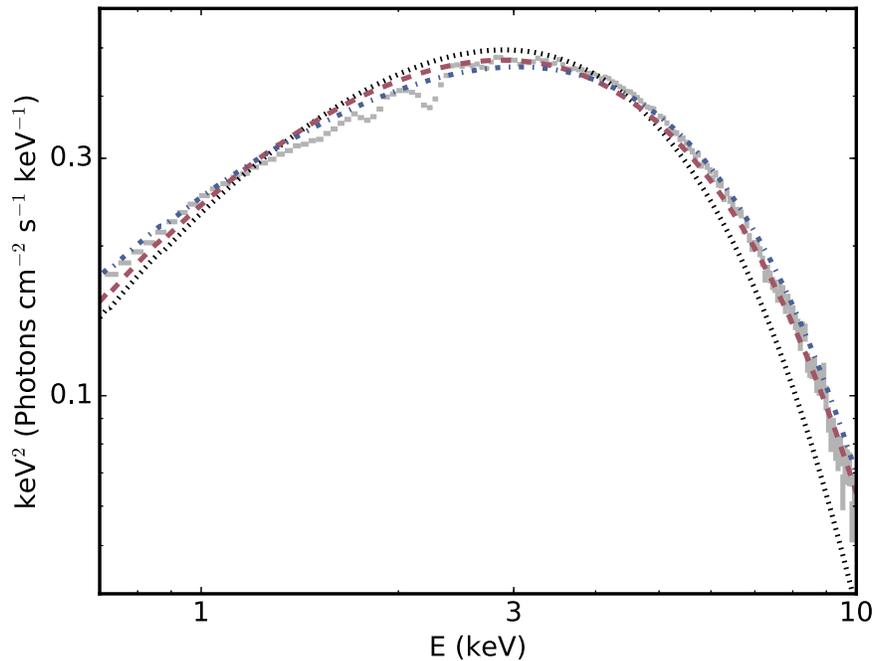
Figure 7. Spectrum from LMC X-3 *XMM*-1, which is shown as an example of a TD BHB spectum that is broader than expected for a thin disk. The spectrum is overplotted with the three disk models used in this paper. These are (in order of increasing breadth) an MCD (black dotted line), KERRBB (red dashed line), and a *p*-free disk (blue dot-dashed line). Clearly the MCD and KERRBB spectral models are insufficiently broad, and a broader spectrum, such as the *p*-free disk, improves the fit.

luminosity at the required temperature, but not to produce the spectral curvature. Using M31 ULX1 as an example, holding the black hole mass fixed at the fitted value and allowing the spin to assume values of $a = 0.9$, 0.5, and 0 results in the 0.3–10 keV unabsorbed luminosity being reduced to $\sim$6, 2, and 1×10^{38} erg s^{-1}, respectively. On the other hand, the lack of lower-spin BHs in the ULX sample could feasibly be a selection effect, since lower-spin objects would also be softer and less efficient and hence require higher (and presumably rarer) mass accretion rates to be classified as ULXs.

Since it is arguably unlikely that all of the BD ULXs contain unusually large stellar remnant black holes with extremely high spins, we instead consider the possibility that BD ULXs are a high Eddington ratio extension of the standard stellar-mass X-ray binaries exemplified by the sample of BHBs. Then, why are the spectra of these two populations so similar? Recently, Straub et al. (2013) showed that the spectral shape of M31 ULX1 remained nearly unchanged over a range of luminosities from $l \sim 0.3$ to $\sim$0.9 and, moreover, differed only slightly from the standard thin-disk model. We also find no clear evidence that the BD ULXs are significantly broader than the BHB spectra, so the BD ULXs could be close to $l \sim 1$ while the BHBs are nearer to $l \sim 0.1$–0.4. This suggests that there may be some important physics missing from the disk models at low l that accounts for the broadening. That is, the progression between the TD BHBs and BD ULXs cannot simply be explained by an initially thin accretion disk becoming geometrically slim and advection dominated. Instead, at face value, these results suggest that the reported BHBs somehow conspire to remain slim down to low l.

Recent radiation magnetohydrodynamical simulations show that a disk at $l \sim 0.8$ can be thermally stabilized by magnetic pressure for an initial (net vertical flux) quadrupole field (Sądowski 2016). The magnetic pressure is larger than the thermal (dominated by radiation) pressure, so the disk has a somewhat larger scale height than predicted from the Shakura–Sunyaev model. This will lower the density of the disk, which reduces the opacity and gives a larger color temperature correction to the emitted spectrum. There are some stringent observational constraints on the average color temperature correction and its constancy with luminosity (Done & Davis 2008), but it may be possible to produce the observed subtle disk broadening. Alternatively, magnetically driven winds may quench energy from the disk (Miller et al. 2006). Still, in either scenario radiation pressure would have to smoothly take over from magnetic pressure/winds to produce the similar observed broadened accretion disk spectra in both low-l BHBs and $l \sim 1$ BD ULXs.

6. Conclusions

We have presented an X-ray spectral and timing study comparing samples of BD ULXs, which are thought to be accreting at around the Eddington rate, with relatively luminous but sub-Eddington TD BHBs. At least some of these TD BHBs exhibit BD-like spectra in the 0.3–10 keV band but at order of magnitude lower luminosities than the ULXs. While it is tempting to speculate that these BHBs and ULXs are accreting at similar Eddington ratios, this would imply near-maximally spinning massive stellar black holes in the BD ULXs, which cannot be trivially produced. Instead, if the BD ULXs are at $l \sim 1$, then the spectral broadening can feasibly be explained by advection in radiation-pressure-dominated, geometrically slim disks. However, this cannot be the case in the TD BHBs as the Eddington ratios are constrained to moderate values. Instead, this implies that some other physical mechanism, such as magnetic pressure, takes over from radiation pressure to produce broad spectra at lower Eddington ratios.

References

Abbott, B. P., Abbott, R., Abbott, T. D., et al. 2016, PhRvL, 116, 061102
Abramowicz, M. A., Czerny, B., Lasota, J. P., & Szuszkiewicz, E. 1988, ApJ, 332, 646
Akyuz, A., Kayaci, S., Avdan, H., et al. 2013, AJ, 145, 67
Alam, M. S., Dewangan, G. C., Belloni, T., Mukherjee, D., & Jhingan, S. 2014, MNRAS, 445, 4259
Arnaud, K. A. 1996, in ASP Conf. Ser. 101, Astronomical Data Analysis Software and Systems V, ed. G. H. Jacoby & J. Barnes (San Francisco, CA: ASP), 17
Bachetti, M., Harrison, F. A., Walton, D. J., et al. 2014, Natur, 514, 202
Bachetti, M., Rana, V., Walton, D., et al. 2013, ApJ, 778, 163
Balucinska-Church, M., & McCammon, D. 1992, ApJ, 400, 699
Bardeen, J. M. 1970, Natur, 226, 64
Barnard, R., Garcia, M., & Murray, S. S. 2013, ApJ, 772, 126
Belczynski, K., Heger, A., Gladysz, W., et al. 2016, A&A, 594, A97
Chen, T. 2011, in IAU Symp. 275, Jets at all Scales, ed. G. E. Romero, R. A. Sunyaev, & T. Bellon (Cambridge: Cambridge Univ. Press), 327
Crandall, S., & Ratra, B. 2015, ApJ, 815, 87
Davis, S. W., Blaes, O. M., Hubeny, I., & Turner, N. J. 2005, ApJ, 621, 372
de Grijs, R., Wicker, J. E., & Bono, G. 2014, AJ, 147, 122
De Marco, B., Ponti, G., Miniutti, G., et al. 2013, MNRAS, 436, 3782
Dickey, J. M., & Lockman, F. J. 1990, ARA&A, 28, 215
Done, C., & Davis, S. W. 2008, ApJ, 683, 389
Done, C., & Diaz Trigo, M. 2010, MNRAS, 407, 2287
Done, C., Gierliński, M., & Kubota, A. 2007, A&ARv, 15, 1
Dunn, R. J. H., Fender, R. P., Körding, E. G., Belloni, T., & Cabanac, C. 2010, MNRAS, 403, 61
Ebisawa, K. 1998, in IAU Symp. 188, The Hot Universe, ed. K. Koyama, S. Kitamoto, & M. Itoh (Dordrecht: Kluwer Academic), 392
Feng, H., & Kaaret, P. 2009, ApJ, 696, 1712
Fragos, T., & McClintock, J. E. 2015, ApJ, 800, 17
Fuerst, F., Walton, D. J., Harrison, F. A., et al. 2016, ApJL, 831, 14
Gammie, C. F., Shapiro, S. L., & McKinney, J. C. 2004, ApJ, 602, 312
Gierliński, M., Done, C., & Page, K. 2008, MNRAS, 388, 753
Gierliński, M., Done, C., & Page, K. 2009, MNRAS, 392, 1106
Gladstone, J. C., Roberts, T. P., & Done, C. 2009, MNRAS, 397, 1836
Gou, L., McClintock, J. E., Liu, J., et al. 2009, ApJ, 701, 1076
Heil, L. M., & Vaughan, S. 2010, MNRAS, 405, L86
Hernández-García, L., Vaughan, S., Roberts, T. P., & Middleton, M. 2015, MNRAS, 453, 2877
Hui, Y., & Krolik, J. H. 2008, ApJ, 679, 1405
Hynes, R. I., Steeghs, D., Casares, J., Charles, P. A., & O'Brien, K. 2003, ApJL, 583, L95
Israel, G. L., Belfiore, A., Stella, L., et al. 2016a, arXiv:1609.07375
Israel, G. L., Papitto, A., Esposito, P., et al. 2016b, arXiv:1609.06538
Kaaret, P., & Corbel, S. 2009, ApJ, 697, 950
Kaur, A., Henze, M., Haberl, F., et al. 2012, A&A, 538, A49
King, A. R., Davies, M. B., Ward, M. J., Fabbiano, G., & Elvis, M. 2001, ApJL, 552, L109

King, A. R., & Kolb, U. 1999, MNRAS, 305, 654
Kirsch, M. G. F., Schönherr, G., Kendziorra, E., et al. 2006, A&A, 453, 173
Kolehmainen, M., & Done, C. 2010, MNRAS, 406, 2206
Kolehmainen, M., Done, C., & Díaz Trigo, M. 2011, MNRAS, 416, 311
Kubota, A., Done, C., Davis, S. W., et al. 2010, ApJ, 714, 860
Kubota, A., & Makishima, K. 2004, ApJ, 601, 428
Kubota, A., Tanaka, Y., Makishima, K., et al. 1998, PASJ, 50, 667
La Parola, V., D'Aí, A., Cusumano, G., & Mineo, T. 2015, A&A, 580, A71
La Parola, V., Damiani, F., Fabbiano, G., & Peres, G. 2003, ApJ, 583, 758
Ludlam, R. M., Miller, J. M., & Cackett, E. M. 2015, ApJ, 806, 262
Marchant, P., Langer, N., Podsiadlowski, P., Tauris, T. M., & Moriya, T. J. 2016, A&A, 588, A50
McClintock, J. E., Narayan, R., & Steiner, J. F. 2014, SSRv, 183, 295
McClintock, J. E., & Remillard, R. A. 2006, in Compact Stellar X-ray Sources, ed. W. H. G. Lewin & M. van der Klis (Cambridge: Cambridge Univ. Press), 157
McClintock, J. E., Shafee, R., Narayan, R., et al. 2006, ApJ, 652, 518
Middleton, M. 2016, in Astrophysics of Black Holes, ed. C. Bambi (Berlin Heidelberg: Springer-Verlag), 99
Middleton, M. J., Miller-Jones, J. C. A., Markoff, S., et al. 2013, Natur, 493, 187
Middleton, M. J., Sutton, A. D., & Roberts, T. P. 2011, MNRAS, 417, 464
Middleton, M. J., Sutton, A. D., Roberts, T. P., Jackson, F. E., & Done, C. 2012, MNRAS, 420, 2969
Middleton, M. J., Walton, D. J., Roberts, T. P., & Heil, L. 2014, MNRAS, 438, L51
Migliari, S., & Fender, R. P. 2006, MNRAS, 366, 79
Miller, J. M., Fabian, A. C., & Miller, M. C. 2004, ApJ, 607, 931
Miller, J. M., Raymond, J., Fabian, A., et al. 2006, Natur, 441, 953
Miller, J. M., Reynolds, C. S., Fabian, A. C., et al. 2008, ApJL, 679, L113
Ng, C., Díaz Trigo, M., Cadolle Bel, M., & Migliari, S. 2010, A&A, 522, A96
Orosz, J. A., Steeghs, D., McClintock, J. E., et al. 2009, ApJ, 697, 573
Orosz, J. A., Steiner, J. F., McClintock, J. E., et al. 2014, ApJ, 794, 154
Owen, R. A., & Warwick, R. S. 2010, MNRAS, 403, 558
Pietrzyński, G., Graczyk, D., Gieren, W., et al. 2013, Natur, 495, 76
Plant, D. S., Fender, R. P., Ponti, G., Muñoz-Darias, T., & Coriat, M. 2014, MNRAS, 442, 1767
Podsiadlowski, P., Rappaport, S., & Han, Z. 2003, MNRAS, 341, 385
Reis, R. C., Fabian, A. C., Ross, R. R., et al. 2008, MNRAS, 387, 1489
Remillard, R. A., & McClintock, J. E. 2006, ARA&A, 44, 49
Ruhlen, L., & Smith, D. M. 2010, BAAS, 42, 672
Sądowski, A. 2009, ApJS, 183, 171
Sądowski, A. 2016, MNRAS, 459, 4397
Schlegel, E. M., & Pannuti, T. G. 2003, AJ, 125, 3025
Shakura, N. I., & Sunyaev, R. A. 1973, A&A, 24, 337
Shimura, T., & Takahara, F. 1995, ApJ, 445, 780
Soria, R., Wu, K., Page, M. J., & Sakelliou, I. 2001, A&A, 365, L273
Steiner, J. F., McClintock, J. E., Orosz, J. A., et al. 2014, ApJL, 793, L29
Steiner, J. F., McClintock, J. E., Remillard, R. A., et al. 2010, ApJL, 718, L117
Steiner, J. F., Narayan, R., McClintock, J. E., & Ebisawa, K. 2009, PASP, 121, 1279
Stobbart, A.-M., Roberts, T. P., & Wilms, J. 2006, MNRAS, 368, 397
Straub, O., Bursa, M., Sądowski, A., et al. 2011, A&A, 533, A67
Straub, O., Done, C., & Middleton, M. 2013, A&A, 553, A61
Sutton, A. D., Done, C., & Roberts, T. P. 2014, MNRAS, 444, 2415
Sutton, A. D., Roberts, T. P., & Middleton, M. J. 2013, MNRAS, 435, 1758
Swartz, D. A., Ghosh, K. K., Tennant, A. F., & Wu, K. 2004, ApJS, 154, 519
Uttley, P., & Klein-Wolt, M. 2015, MNRAS, 451, 475
Vaughan, S., Edelson, R., Warwick, R. S., & Uttley, P. 2003, MNRAS, 345, 1271
Vierdayanti, K., Watarai, K.-Y., & Mineshige, S. 2008, PASJ, 60, 653
Vulic, N., Gallagher, S. C., & Barmby, P. 2016, MNRAS, 461, 3443
Walton, D. J., Harrison, F. A., Grefenstette, B. W., et al. 2014, ApJ, 793, 21
Watarai, K.-Y., Mizuno, T., & Mineshige, S. 2001, ApJL, 549, L77
Wilkinson, T., & Uttley, P. 2009, MNRAS, 397, 666
Wilms, J., Allen, A., & McCray, R. 2000, ApJ, 542, 914
Yan, M., Sadeghpour, H. R., & Dalgarno, A. 1998, ApJ, 496, 1044
Zdziarski, A. A., Gierliński, M., Mikołajewska, J., et al. 2004, MNRAS, 351, 791
Zhang, S.-N. 2013, FrPhy, 8, 630